



# Instability and symmetry breaking of surfactant films over an air bubble

Xingyi Shi<sup>1</sup>, Gerald G. Fuller<sup>1</sup> and Eric S.G. Shaqfeh<sup>1,2,†</sup>

<sup>1</sup>Department of Chemical Engineering, Stanford University, Stanford, CA 94305, USA

<sup>2</sup>Department of Mechanical Engineering, Stanford University, Stanford, CA 94305, USA

(Received 25 January 2022; revised 11 October 2022; accepted 16 October 2022)

We examine the asymmetric flows of aqueous surfactant films over an air bubble. A thin film is formed by raising an equilibrated air bubble through an aqueous solution of Triton X-100 (0.01 mM, below critical micelle concentration). Due to the advection generated by the squeezing motion, the initially uniformly distributed surfactants redistribute and, thus, generate an axisymmetric surface tension gradient that drives a Marangoni flow. The external forcing of raising the bubble also creates an axisymmetric dimpled film with a radial thickness variation that reaches its minimum at the rim of the dimple. The curvature in the film thickness generates an axisymmetric capillary pressure driven flow. When the apex of the bubble has penetrated the initially flat air-solution interface, the rising bubble is stopped and the resulting flow demonstrates symmetry breaking both in the experiment and in the parameter matched numerical simulation. Linear stability analysis reveals the mechanism behind the disturbance growth. It is found that the most dangerous azimuthal wavenumber scales linearly with the ratio of the rim radius to the radial width of significant radial pressure and surface tension gradients after stopping the bubble. Finally, we compare this instability to the previously studied surfactant spreading induced fingering phenomenon (Warner, Craster & Matar, *Phys. Fluids*, vol. 16, issue 8, 2004, pp. 2933–2951).

**Key words:** lubrication theory

## 1. Introduction

Surfactants are surface active agents that exist between phases to reduce the interfacial energy and thereby stabilize interfaces that are otherwise unstable. They are present in numerous processes that affect our lives. Pulmonary surfactants coat the air-liquid interface of the alveoli and enable us to breathe (Zasadzinski *et al.* 2001). Excessive amounts of insoluble surfactants on the ocean surface can lead to the formation of a visible

† Email address for correspondence: [esgs@stanford.edu](mailto:esgs@stanford.edu)

layer of 'slick' that changes the viscoelasticity of the liquid–air interface and dampen waves (Cunliffe *et al.* 2013). Water-based paints require surfactants to improve wetting and disperse pigments (Hellgren, Weissenborn & Holmberg 1999). Surfactant-based dispersants are used as a chemical means of cleaning an oil spill and preventing the formation of oil slicks (Dave & Ghaly 2011). The prevalence and importance of surfactants call for a fundamental understanding of their dynamical interactions at the interfaces of different materials, and this is a subject of much historical and present day active interest.

The nature of surfactants restricts these amphiphilic molecules to be most active at air–water or oil–water interfaces. Thin liquid films, therefore, are effective systems through which we can examine the dynamics of surfactants. There are several commonly used experimental techniques for generating thin films in surfactant solutions. One technique involves using a syringe to inject air just below a surfactant solution surface to generate a near-hemispherical bubble, whose film thickness at the apex can be measured via interferometric techniques (Champougny *et al.* 2016).

With this method, one can easily study the film drainage rate and the relative importance of gravity to surface tension by changing the bubble volume (Lhuissier & Villermaux 2012). This technique allows researchers to examine the film evolution of large surface bubbles. Miguet *et al.* (2021) studied the marginal regeneration phenomenon of surfactant films over bubbles with a radius of curvature of more than a centimetre. A characteristic visual example of this phenomenon can be found in figure 1 of Miguet *et al.* (2021). Numerous numerical studies of free surface bubbles have been conducted (Pigeonneau & Sellier 2011; Atasi *et al.* 2020). Atasi *et al.* (2020) studied the lifetime of surface bubbles in the presence of surfactants. The numerical study offers many insights into the relations between the evolution of film thickness, gravitational effects and surfactant coverage. However, the study is limited to axisymmetric film evolution and cannot capture the azimuthal flow inside the liquid film that coats the surface bubbles.

A second experimental approach introduces an air bubble at a distance from the interface between a surfactant solution bath and the ambient air. As the air bubble rises, its velocity (Borkowski, Kosior & Zawala 2020) and path (Tagawa, Takagi & Matsumoto 2014) can be studied. A third class of approaches involves mechanically forcing two interfaces close together. This can be achieved through a variety of geometric arrangements, summarized in figure 2 of Chatzigiannakis, Jaensson & Vermant (2021). When this class of thin film generation technique is paired with digital imaging, one can obtain interferometric information on the temporal and spatial evolution of film thickness and symmetry. To set context, we introduce a few examples that are relevant to the present work.

Joye (1994) conducted film drainage experiments with a Scheludko-cell based design, where a thin film is formed by withdrawing liquid from an initially filled circular sample holder. Once the thin film has reached a desired thickness, the withdrawal is stopped and the film is allowed to evolve under various physical forces. An example of asymmetrical, aqueous surfactant film evolution can be found in figure IV-1 of Joye (1994). More recently, this type of apparatus has been improved to study the stratification of foam films (Ochoa *et al.* 2021).

The dynamic fluid–film interferometer (DFI) is another technique used to manually form a thin film (Frostad *et al.* 2016). In the DFI an air bubble or a liquid droplet is supported on a capillary and is fully submerged in a liquid chamber of interest. A motor brings the initially curved and flat faces together until the film is thin enough to form interference patterns. The interference video gives information on film thickness and film symmetry. This set-up has been used to visualize the flow of aqueous surfactant films. Frostad *et al.* (2016) examine three commonly studied water-soluble surfactants (sodium dodecyl sulfate (SDS), cetrimonium bromide (CTAB) and Triton X-100), and their effects on aqueous

surfactant films trapped in between an air bubble and the initially planar air–solution interface. The interference videos for all three species can be found in the supplementary files. In all three videos, the evolution of the film symmetry undergoes similar stages. In the first stage, the field of view of the interference patterns grows radially outward in an axisymmetric fashion. During this stage, the motor is forcing the two interfaces together, forming a dimple atop the air bubble. When the motor stops moving, the dimple ceases to expand in the radial direction, and the system succumbs to ambient disturbances. The disturbance first manifests itself around the rim of the dimple: at 2 s in the SDS video, at 4 s in the CTAB video and at 3 s in the Triton video. Thereafter, the asymmetry grows more pronounced and the previously axisymmetric dimple evolves to conform to the asymmetry at the rim. Eventually, the dimple discharges through a few contact points along the rim and the volume of the dimple drastically decreases. The dimple discharge event triggers secondary non-axisymmetric film evolution until the film thins down to nanoscopic thickness and the bubble coalesces. Understanding the physical forces that drive the onset of the disturbances in the surfactant film is of paramount importance because the symmetry breaking event triggers the subsequent rapid dimple discharge that contributes to drastic film thinning that affects the lifetime of the bubble. Highly asymmetrical patterns of insoluble surfactant films can be seen in figure 9 of Hermans *et al.* (2015) and figures 6 and 7 of Bhamla *et al.* (2017). Additional experimental examples of asymmetrical dynamic evolution of thin films are discussed in our previous work (Shi *et al.* 2021).

These examples of asymmetrical interference patterns suggest that there are common forces associated with surfactant film evolution that drive the system to develop in an asymmetrical fashion. To this end, we devote the present study to understanding the physical mechanism behind the asymmetrical evolution of water-soluble surfactant films, at a concentration below the critical micelle concentration. The article is organized as follows. We first introduce in detail the DFI set-up and the experimental procedures used for this study, followed by descriptions of the lubrication theory and the numerical methods. We then describe the experimental and computational evolution of an aqueous surfactant film over an air bubble, with a focus on capturing the onset of asymmetric disturbances. A linear stability analysis is presented to elucidate the mechanism behind the observed symmetry breaking events. The analysis also reveals mode selection for a given set of system parameters. We finish the article with a discussion of the factors that affect the mode selection and the mechanism of the instability.

## 2. Experiment

Surfactant film drainage experiments are conducted using a custom-made DFI. The equipment set-up is described in our previous work (Shi, Fuller & Shaqfeh 2020). For completeness, we shall only provide a succinct description of the apparatus and the experimental procedures.

The experimental apparatus is composed of a liquid sample chamber, which is mounted onto a motorized platform. Two of the four chamber walls are made of glass, enabling visualization into the chamber. A 16-gauge capillary with an inner diameter of 1.2 mm is held fixed and positioned at the centre of the chamber at the start of an experiment. The capillary is connected to a 100  $\mu\text{l}$  syringe filled with air.

Prior to each sample loading, the cleanliness of the assembly is tested via the following procedure. The empty chamber is filled with deionized water and an air bubble of approximately 5  $\mu\text{l}$  is extruded from the capillary. The motorized platform then

positions the apex of the bubble to be approximately 0.1 mm away from the air–water interface. The motor then translates the chamber downward for 0.4 mm at  $0.1 \text{ mm s}^{-1}$ . If the bubble coalesces within 5 s, then the chamber is deemed sufficiently clean and experiments with surfactant solutions may proceed. The cutoff time of 5 s is chosen because a surfactant-covered bubble that undergoes the same experimental procedure typically lasts longer than 12 s. If the bubble in the deionized water takes longer than 5 s to coalesce, then the chamber is taken from the platform and vigorously cleaned with deionized water. The test and cleaning are repeated until the assembly meets the criterion.

The model surfactant used in this study is Triton X-100, a widely studied non-ionic surfactant composed of a hydrophilic polyethylene oxide chain and a hydrophobic hydrocarbon chain. Furthermore, Triton X-100 readily adsorbs onto air–water interfaces, making it one of the more effective, water-soluble surfactants (Chang & Franses 1995). For a typical experiment, approximately 4 ml of a Triton X-100 (laboratory grade, Sigma-Aldrich) aqueous solution is loaded into the chamber. The water used in making the solution is filtered by a Millipak Express 40 filter ( $0.22 \mu\text{m}$  membrane) to remove particulates. For all the experiments presented in this paper, the concentration of the Triton X-100 solution is  $0.01 \text{ mmol l}^{-1}$ , which is below the critical micelle concentration at  $25^\circ\text{C}$  (Lin, McKeigue & Maldarelli 1990). An air bubble of approximately  $5 \mu\text{l}$  is extruded from the capillary. The top of the chamber is then covered with a glass slide and the system is left to equilibrate for 30 min, such that the surfactant present in the bulk can adsorb onto the newly formed air bubble.

After the equilibration period, the glass cover is removed and the motorized platform moves the chamber downward such that the apex of the bubble is positioned as close as possible to the flat liquid–air interface without penetrating the interface (approximately 0.1 mm of apex clearance). This procedure ensures the applicability of lubrication theory, developed to describe the dynamics of the film. After a one minute pause, the motor moves the chamber assembly downward by 0.4 mm at a speed of  $0.1 \text{ mm s}^{-1}$ . The motor then stops the translation. The top camera records the interference patterns of the thin liquid film atop the air bubble throughout this process. Film thickness and symmetry information are obtained by analysing the interference video.

### 3. Theoretical model

#### 3.1. Lubrication equations

We consider a spherical, non-deformable air bubble of radius  $a$ , approaching an initially flat interface between air and an aqueous surfactant solution (figure 1). At the start of the experiment, the apex of the bubble is positioned a distance  $b$  below the top air–liquid interface. It is assumed that  $\epsilon \equiv b/a \ll 1$ , such that the lubrication approximation applies. The bulk liquid phase is composed of an aqueous surfactant solution with a bulk surfactant concentration of  $c_0$ . We assume that at the start of the experiment, the surfactant in the solution and the surfactant adsorbed onto the two air–liquid interfaces are in equilibrium and the equilibrium surface concentration is  $\Gamma_0$ . The surfactant is characterized by a bulk diffusivity of  $D$  and a surface diffusivity of  $D_s$ . The bulk concentration of the surfactant is below the critical micelle concentration and is small enough such that the solution density and viscosity are the same as those of the Newtonian solvent,  $\rho$  and  $\mu$ , respectively. At  $t^* = 0$ , the bubble is moved upwards, against gravity, for a distance  $d$  at a speed of  $U$ . The bubble is then held fixed after  $t_{\text{stop}}^* = d/U$ . For simplicity, the capillary-pinned bubble in the experiment is treated in the theoretical model as a non-deformable sphere with a

## Instability of surfactant films

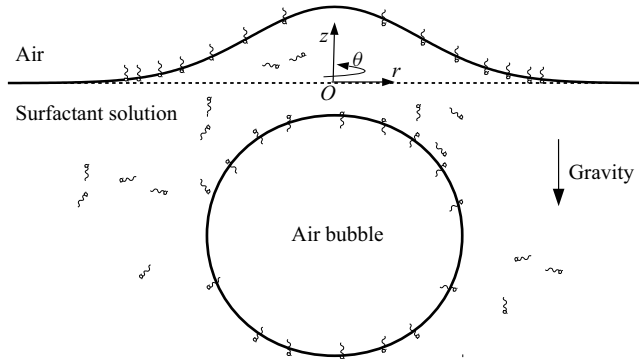


Figure 1. Schematic of a spherical air bubble approaching the interface between air and aqueous surfactant solution.

non-zero surface velocity. As shown in later sections, this simplifying assumption still allows us to capture the onset of symmetry breaking. Furthermore, because the Reynolds number  $Re \equiv (\rho Ub)/\mu \ll 1$ , we neglect all inertial effects. We also neglect the effects of evaporation-driven film thinning and evaporation-generated Marangoni flows (Poulain, Villermaux & Bourouiba 2018) to focus on the effects of surfactant transport-induced phenomena. As will be shown in the results section, the model is only used to capture the dynamics during the onset of the disturbance. During this time, the minimum film thickness is around 200 nm, thus, we neglect the effects of the disjoining pressure (Stubenrauch & Von Klitzing 2003).

A cylindrical coordinate system  $(z^*, r^*, \theta)$  is used to accommodate the geometry of the system and the motion of the bubble. The origin is placed at the intersection of the initially flat liquid–air interface and the vertical axis of the bubble. The vertical axis is represented by  $z^*$ , the radial coordinate is represented by  $r^*$  and  $\theta$  represents the azimuthal angle. The asterisk represents dimensional quantities.

The following scales are chosen to render the governing equations dimensionless. The lubrication length scales in the axial and radial directions are  $b$  and  $\sqrt{ab}$ , respectively. The vertical velocity ( $v_z^*$ ) is scaled by the motor speed ( $U$ ). Mass conservation demands the velocities in the radial ( $v_r^*$ ) and azimuthal ( $v_\theta^*$ ) directions be scaled by  $U/\sqrt{\epsilon}$ . Time is non-dimensionalized by  $b/U$  and the pressure scale is  $(1/\epsilon^2)(\mu U/a)$ . The scale for the bulk surfactant molar concentration is  $c_0$ . The surface adsorbed surfactant concentration ( $\Gamma^*$ ) is non-dimensionalized by the maximum packing concentration ( $\Gamma_\infty$ ). The scale for surfactant adsorption fluxes ( $(U\Gamma_\infty)/b$ ) is obtained when non-dimensionalizing the mass transfer equation of the surface adsorbed species.

With the above scales, we proceed to non-dimensionalize the governing equations, expand all variables in  $\epsilon$ :  $\psi = \psi^{(0)} + \epsilon\psi^{(1)} + \epsilon^2\psi^{(2)} + \dots$  and extract the governing equations for variables at each order. Similar to our previous study (Shi *et al.* 2020), we need to examine the combined effects of the  $O(1)$  and the  $O(\epsilon)$  terms, such that when the concentration of the surfactant goes to zero, the governing equations of a clean air–liquid interface are recovered. The order-combined variables are denoted with a hat:  $\hat{\psi} \equiv \psi^{(0)} + \epsilon\psi^{(1)}$ . We introduce only the final form of the governing equations. Detailed treatment of the order-combined variables can be found in the Appendix of Shi *et al.* (2020) and § A.7.3 of Barakat (2018).

The position of the top liquid–air interface ( $\hat{h}_1$ ) is described by

$$\frac{\partial \hat{h}_1}{\partial t} + \frac{1}{r} \frac{\partial}{\partial r} \left( r \hat{h}_1 \langle v_r \rangle \right) + \frac{1}{r} \frac{\partial}{\partial \theta} \left( \hat{h}_1 \langle v_\theta \rangle \right) = \begin{cases} 1, & (t \leq t_{stop}), \\ 0, & (t > t_{stop}), \end{cases} \quad (3.1)$$

where  $\hat{h} \equiv \hat{h}_1 - h_2$  and  $t_{stop} \equiv d/b$ . The position of the bubble–liquid interface ( $h_2$ ) is known at all times, as we assume no bubble deformation, i.e.

$$h_2 \equiv \begin{cases} -1 - r^2/2 + t, & (t \leq t_{stop}), \\ -1 - r^2/2 + t_{stop}, & (t > t_{stop}). \end{cases} \quad (3.2)$$

The bracket around the radial and azimuthal velocities indicates depth averaging:  $\langle \hat{\psi} \rangle \equiv (1/\hat{h}) \int_{h_2}^{\hat{h}_1} \hat{\psi} dz$ , where  $\psi = v_r$  and  $v_\theta$ . The normal stress balance across the top liquid–air interface is

$$\frac{1}{r} \frac{\partial}{\partial r} \left( r \frac{\partial \hat{h}_1}{\partial r} \right) + \frac{1}{r^2} \frac{\partial^2 \hat{h}_1}{\partial \theta^2} - Bo \hat{h}_1 + Ca \hat{P} + 2\epsilon Ca \left( \frac{1}{r} \frac{\partial}{\partial r} \left( r \langle v_r \rangle \right) + \frac{1}{r} \frac{\partial \langle v_\theta \rangle}{\partial \theta} \right) = 0, \quad (3.3)$$

where  $Bo \equiv \rho g a b / \gamma_{water}$  and  $Ca \equiv (1/\epsilon^2)(\mu U / \gamma_{water})$ . The gravitational acceleration is denoted by  $g = 9.8 \text{ m s}^{-2}$ . The first non-dimensional parameter is the Bond number, which compares the relative importance of gravity to the surface tension of a clean interface. The second non-dimensional number is the capillary number, which compares viscous stresses to capillary stresses. The tangential stress balances in the radial and azimuthal directions are

$$\begin{aligned} \frac{\partial \hat{P}}{\partial r} = & \frac{1}{\hat{h}} \frac{1}{\epsilon Ca} \left( \frac{\partial (-\Pi_1^{(0)})}{\partial r} + \frac{\partial (-\Pi_2^{(0)})}{\partial r} \right) \\ & + \epsilon \left\{ 2 \frac{\partial}{\partial r} \left( \frac{1}{r} \frac{\partial}{\partial r} \left( r \langle v_r \rangle \right) \right) + \frac{\partial}{\partial r} \left( \frac{1}{r} \frac{\partial \langle v_\theta \rangle}{\partial \theta} \right) + \frac{1}{r^2} \frac{\partial^2 \langle v_r \rangle}{\partial \theta^2} - \frac{2}{r^2} \frac{\partial \langle v_\theta \rangle}{\partial \theta} \right. \\ & \left. + \frac{2}{\hat{h}} \frac{\partial \hat{h}}{\partial r} \left( \frac{1}{r} \frac{\partial}{\partial r} \left( r \langle v_r \rangle \right) + \frac{\partial \langle v_r \rangle}{\partial r} + \frac{1}{r} \frac{\partial \langle v_\theta \rangle}{\partial \theta} \right) + \frac{1}{\hat{h}} \frac{1}{r} \frac{\partial \hat{h}}{\partial \theta} \left( \frac{1}{r} \frac{\partial \langle v_r \rangle}{\partial \theta} + r \frac{\partial}{\partial r} \left( \frac{\langle v_\theta \rangle}{r} \right) \right) \right\} \end{aligned} \quad (3.4)$$

and

$$\begin{aligned} \frac{1}{r} \frac{\partial \hat{P}}{\partial \theta} = & \frac{1}{\hat{h}} \frac{1}{\epsilon Ca} \left( \frac{1}{r} \frac{\partial (-\Pi_1^{(0)})}{\partial \theta} + \frac{1}{r} \frac{\partial (-\Pi_2^{(0)})}{\partial \theta} \right) \\ & + \epsilon \left\{ \frac{2}{r^2} \frac{\partial^2 \langle v_\theta \rangle}{\partial \theta^2} + \frac{\partial}{\partial r} \left( \frac{1}{r} \frac{\partial}{\partial r} \left( r \langle v_\theta \rangle \right) \right) + \frac{1}{r} \frac{\partial}{\partial \theta} \left( \frac{1}{r} \frac{\partial}{\partial r} \left( r \langle v_r \rangle \right) \right) + \frac{2}{r^2} \frac{\partial \langle v_r \rangle}{\partial \theta} \right. \\ & \left. + \frac{2}{\hat{h}} \frac{1}{r} \frac{\partial \hat{h}}{\partial \theta} \left( \frac{1}{r} \frac{\partial}{\partial r} \left( r \langle v_r \rangle \right) + \frac{\langle v_r \rangle}{r} + \frac{2}{r} \frac{\partial \langle v_\theta \rangle}{\partial \theta} \right) + \frac{1}{\hat{h}} \frac{\partial \hat{h}}{\partial r} \left( \frac{1}{r} \frac{\partial \langle v_r \rangle}{\partial \theta} + r \frac{\partial}{\partial r} \left( \frac{\langle v_\theta \rangle}{r} \right) \right) \right\}, \end{aligned} \quad (3.5)$$

where  $\Pi_1^{(0)}$  and  $\Pi_2^{(0)}$  are the surface pressures exerted by the adsorbed surfactant on the top and bottom interfaces, respectively. The surface pressures represent the



reduction in surface tension caused by the presence of the surfactant on the interfaces. Non-dimensionalizing surface tension with  $\gamma_{water} = 72 \text{ mN m}^{-1}$  we obtain  $\gamma_1 = 1 - \Pi_1^{(0)}$  and  $\gamma_2 = 1 - \Pi_2^{(0)}$ .

At  $t = 0$ , the bulk surfactant and the adsorbed surfactant are assumed to be in equilibrium and the adsorbed surfactant concentration is assumed to be  $\Gamma_0$  on both interfaces, despite the difference in the curvature of the two interfaces. Based on this assumption and by letting  $\Gamma_1^{(0)}$  and  $\Gamma_2^{(0)}$  have the same boundary conditions, we further simplify the equations  $\Gamma_1^{(0)} = \Gamma_2^{(0)} \equiv \Gamma^{(0)}$ . Consequently, the flux of surfactant adsorbing from the bulk onto the two interfaces are the same, i.e.  $j_{n1} = j_{n2} \equiv j_n$ , and the surface pressures are the same, i.e.  $\Pi_1^{(0)} = \Pi_2^{(0)} \equiv \Pi^{(0)}$ . Without committing to any specific surfactant species, we now express the transport equations for the surfactant species present in the bulk and on the liquid–air interfaces.

$$\begin{aligned} \frac{\partial c^{(0)}}{\partial t} + \langle \widehat{v_r} \rangle \frac{\partial c^{(0)}}{\partial r} + \langle \widehat{v_\theta} \rangle \frac{1}{r} \frac{\partial c^{(0)}}{\partial \theta} - \frac{1}{Pe} \left( \frac{1}{r} \frac{\partial}{\partial r} \left( r \frac{\partial c^{(0)}}{\partial r} \right) + \frac{1}{r^2} \frac{\partial^2 c^{(0)}}{\partial \theta^2} \right) \\ - \frac{1}{Pe} \frac{1}{\hat{h}} \left( \frac{\partial \hat{h}}{\partial r} \frac{\partial c^{(0)}}{\partial r} + \frac{1}{r} \frac{\partial \hat{h}}{\partial \theta} \frac{1}{r} \frac{\partial c^{(0)}}{\partial \theta} \right) = - \frac{2\beta}{\hat{h}} j_n \end{aligned} \tag{3.6}$$

and

$$\begin{aligned} \frac{\partial \Gamma^{(0)}}{\partial t} + \frac{1}{r} \frac{\partial}{\partial r} \left( r \Gamma^{(0)} v_{r,s} \right) + \frac{1}{r} \frac{\partial}{\partial \theta} \left( \Gamma^{(0)} v_{\theta,s} \right) - \frac{1}{Pe_s} \left( \frac{1}{r} \frac{\partial}{\partial r} \left( r \frac{\partial \Gamma^{(0)}}{\partial r} \right) + \frac{1}{r^2} \frac{\partial^2 \Gamma^{(0)}}{\partial \theta^2} \right) \\ = j_n, \end{aligned} \tag{3.7}$$

where  $\beta \equiv \Gamma_\infty / (c_0 b)$ . The bulk Péclet number ( $Pe \equiv aU/D$ ) compares convection to bulk diffusion. The surface Péclet number ( $Pe_s \equiv aU/D_s$ ) compares the effects of convection to surface diffusion for the adsorbed surfactants. The surface velocities ( $v_{r,s}$  and  $v_{\theta,s}$ ) can be obtained by integrating the Stokes equations and incorporating the  $O(1)$  tangential stress balances, i.e.

$$v_{r,s} = \langle \widehat{v_r} \rangle - \frac{1}{\epsilon Ca} \frac{\hat{h}}{6} \frac{\partial \Pi^{(0)}}{\partial r} \tag{3.8}$$

and

$$v_{\theta,s} = \langle \widehat{v_\theta} \rangle - \frac{1}{\epsilon Ca} \frac{\hat{h}}{6} \frac{1}{r} \frac{\partial \Pi^{(0)}}{\partial \theta}. \tag{3.9}$$

The corresponding initial and boundary conditions for these equations are

$$\begin{aligned} \text{at } t = 0 : \hat{h}_1 = 0, \quad \hat{P} = 0, \quad \langle \widehat{v_r} \rangle = 0, \quad \langle \widehat{v_\theta} \rangle = 0, \quad c^{(0)} = 1, \quad \Gamma^{(0)} = \Gamma_0 / \Gamma_\infty, \\ \text{as } r \rightarrow \infty : \hat{h}_1 \rightarrow 0, \quad \hat{P} \rightarrow 0, \quad \langle \widehat{v_r} \rangle \rightarrow 0, \quad \langle \widehat{v_\theta} \rangle \rightarrow 0, \quad c^{(0)} \rightarrow 1, \quad \Gamma^{(0)} \rightarrow \Gamma_0 / \Gamma_\infty, \\ \text{and } \psi(\theta) = \psi(\theta + 2\pi), \quad \text{where } \psi = \hat{h}_1, \hat{P}, \langle \widehat{v_r} \rangle, \langle \widehat{v_\theta} \rangle, c^{(0)}, \Gamma^{(0)}. \end{aligned} \tag{3.10}$$

$\epsilon$	$b/a$	0.108
$t_{stop}$	$d/b$	2–8
$Ca$	$(1/\epsilon^2)(\mu U/\gamma_{water})$	$1.2 \times 10^{-4}$
$Bo$	$(\rho g a b)/\gamma_{water}$	0.021
$Pe$	$aU/D$	458
$Pe_s$	$aU/D_s$	4580
$Ma$	$\epsilon RT\Gamma_\infty/(\mu U)$	7665
$La$	$(k_a c_0)/k_d$	15.1
$\alpha$	$(bk_a c_0)/U$	0.644
$\beta$	$\Gamma_\infty/(c_0 b)$	2.26

Table 1. Dimensionless parameters used in this study.

### 3.2. Surfactant specific parameters

The isotherms that relate the surface pressure to the adsorbed surfactant concentration are dependent on the surfactant species. In this section we describe the isotherm and the associated adsorption and desorption fluxes for Triton X-100. Lin *et al.* (1990) published a detailed study of Triton X-100 using a pendant drop tensiometry apparatus. All Triton X-100 associated parameters are extracted from their study. The diffusivity of Triton X-100 in water is  $D = 2.6 \times 10^{-10} \text{ m}^2 \text{ s}^{-1}$ . The surface diffusivity is assumed to be ten times larger than bulk diffusivity. Figure 7 of Lin *et al.* (1990) describes the equilibrium isotherms for Triton X-100 aqueous solutions. There are no significant differences between the Frumkin and Langmuir isotherms for bulk concentrations between 1  $\mu\text{M}$  and 100  $\mu\text{M}$ . In this paper, for the sake of simplicity, we use the Langmuir isotherm

$$\gamma = 1 - \Pi = 1 + \epsilon Ca Ma \log[1 - \Gamma], \quad (3.11)$$

where the Marangoni number is  $Ma \equiv \epsilon RT\Gamma_\infty/(\mu U)$ . After applying the above definition of surface pressure, the Marangoni number appears in the non-dimensionalized radial and azimuthal stress balances. It is a multiplier to the dimensionless concentration whose gradient drives Marangoni flow. Here  $\Gamma_\infty$  is obtained by fitting data to the Langmuir–von Szyszkowski’s equation,  $\gamma = 1 - RT\Gamma_\infty/\gamma_{water} \log[1 + c^*/c_{fit}]$ , yielding  $\Gamma_\infty = 2.91 \times 10^{-6} \text{ mol m}^{-2}$  and  $c_{fit} = 6.62 \times 10^{-4} \text{ mol m}^{-3}$ .

Langmuir kinetics is used to describe the dynamics of surfactant adsorbing onto the air–water interface and the bubble surface. The adsorption flux is defined as  $j_{ads}^* = k_a c^*(\Gamma^* - \Gamma_\infty)$  and the desorption flux is  $j_{des}^* = k_d \Gamma^*$ . The adsorption coefficient,  $k_a = 50 \text{ m}^3 \text{ s}^{-1} \text{ mol}^{-1}$ , is extracted from figure 10 of Lin *et al.* (1990). It follows that the desorption coefficient  $k_d = c_{fit} k_a = 0.033 \text{ s}^{-1}$ . Non-dimensionalizing the total flux of surfactant adsorbing onto an air–water interface we obtain  $j_n \equiv \alpha (c(1 - \Gamma) - \Gamma/La)$ , where  $La \equiv (k_a c_0)/k_d$  and  $\alpha \equiv (bk_a c_0)/U$ . All of the extracted values are also consistent with the values published in table 4 of Shen *et al.* (2002). Table 1 contains a summary of all the non-dimensional parameters and their values used in this study.

### 3.3. Numerical considerations

The set of six nonlinear governing equations describes the relationship among six unknowns. The initial and boundary conditions of four of these are homogeneous. Here  $c^{(0)}$  and  $\Gamma^{(0)}$  are the variables with non-homogeneous initial and boundary conditions. In the numerical implementation, we solve for the respective variables:  $\log(c^{(0)})$



and  $\Gamma^{(0)} - \Gamma_0/\Gamma_\infty$ . The governing equations are spatially discretized using the finite difference method. In the radial mesh a stretched mesh is used such that in each radial direction, 50% of the grid points are positioned on  $r \in [0, 1]$  and the rest of the points are positioned on  $r \in (1, R_{max}]$ . In the azimuthal direction the mesh is evenly divided into 60 slices such that the disturbance onset can be reasonably resolved. A Crank–Nicolson, adaptive time stepping is used for time advancement. At each iteration, the governing equations are solved using a lower–upper (LU) factorization based direct solver provided in the PETSc package (Balay *et al.* 2019). Validation of the numerical solution is discussed in detail in the following sections.

## 4. Results and discussion

### 4.1. Thin film evolution and disturbance onset

Figure 2 shows the validation experimental and simulation data associated with the dynamical evolution of a Triton X-100 aqueous film over an air bubble. The experimental conditions and experimental parameters are presented in table 1 with  $t_{stop} = 3.11$ . Figure 2(a) shows the temporal evolution of the maximum film thickness. For the experimental data,  $\hat{h}_{max}$  is defined to be the maximum measurable film thickness within the field of view, while in the simulation,  $\hat{h}_{max} = \max(\hat{h}(t, r \leq R(\theta), \theta))$ , where  $R(\theta)$  corresponds to the radial position of minimum film thickness for a given azimuthal direction. Here  $R(\theta)$ , the rim, bounds the so-called dimple.

In both the experiment and the simulation,  $\hat{h}_{max}$  decreases with time as a result of the squeezing motion of the motor driving the two interfaces together. Similar to the experiments done by Frostad *et al.* (2016), this experiment also shows three stages of film evolution. The first stage corresponds to the time when the motor is moving:  $0 < t < t_{stop}$ . During this period, the bubble is forced upward and the dimple grows from  $r = 0$  radially outward in an axisymmetric fashion (figure 2b1–3). The second stage corresponds to the rapid change in film thickness after  $t_{stop} = 3.11$  ( $t_{stop} < t < 5$ , figure 2b4–10). Figure 3(a) provides the film thickness contour that corresponds to the interference pattern in figure 2(b4). Shortly after the motor has stopped moving, the system succumbs to ambient disturbances that break the axial symmetry of the outermost blue ring that corresponds to the rim location (figure 2b5). Figure 3(b) shows the effect of the disturbances on the film thickness at  $t = 3.65$ . As the amplitude of the disturbance grows, the thin film becomes more asymmetrical, and the previously centred  $\hat{h}_{max}$  is convected away from  $r = 0$  (figures 2b6–8 and 3c). Eventually, the dimple discharges from the side (figure 2b9 and 2b10), leaving behind a plume of a very non-axisymmetric film (figure 2b11 and 2b12). The film enters the last stage of its evolution, where the non-axisymmetric film continues to thin at a rate that is slowed relative to that during the dimple discharge (figure 2a). The bubble eventually coalesces as a result of further ambient disturbances.

In contrast to the experimental evolution of  $\hat{h}_{max}$ , the simulated maximum film thickness thins at a faster rate during  $0 < t < 1$ , leading to a thinner film during  $1 < t < 4.22$ . We believe the differences are mainly the result of our assumption that the lower surface is non-deformable. This assumption can be evaluated by examining the deformation of a freely rising bubble in a surfactant free liquid (Pigeonneau & Sellier 2011). The Bond number in this study is close to the parameter used in figure 9(a) of Pigeonneau & Sellier (2011), where an air bubble freely rises toward an initially flat liquid–air interface with a one-radius initial clearance over the apex of the bubble. In their study, a small

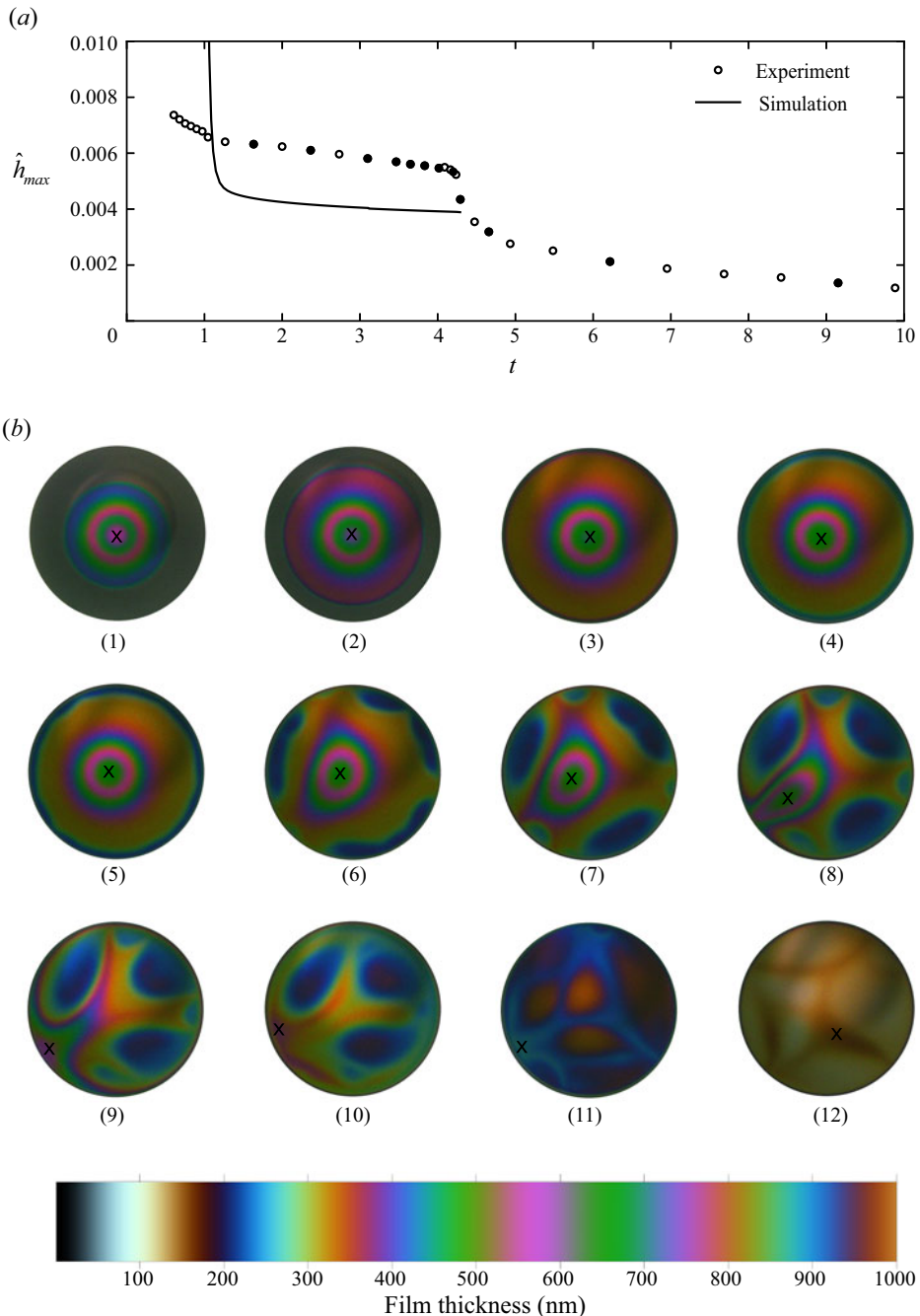


Figure 2. Evolution of a Triton X-100 aqueous film over an air bubble. (a) Dynamics of the maximum film thickness measured in the experiment (circles) and obtained via 2-D numerical simulation (solid line). The experimental parameters and simulation parameters are reported in [table 1](#), with a  $t_{stop} = 3.11$ . The twelve filled circles correspond to the twelve interference patterns displayed in (b). The diameter of each of the interferograms corresponds to 1.2 mm. The location of  $\hat{h}_{max}$  is marked with an 'x'.

## Instability of surfactant films

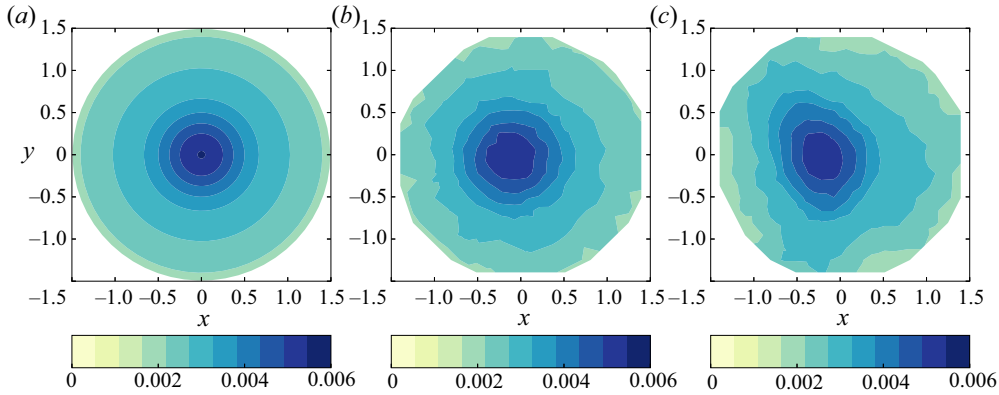


Figure 3. Experimental film thickness profiles during the symmetry breaking event for an aqueous solution of Triton X-100 at a concentration of 0.01 mM; (a)  $t = 3.47$ , (b)  $t = 3.65$ , (c)  $t = 3.83$ . These contour maps correspond to the interference patterns presented in figures 2(b4), (b5) and (b6).

amount of deformation is observed when the bubble freely rises until the minimum film thickness approaches the numerical resolution. In fact, Pigeonneau & Sellier (2011) have deemed the deformation to be small enough such that ‘the bubble remains nearly spherical when rising’. However, in our study, a motor forces the bubble upward, thus moving beyond the position described in figure 9(a) of Pigeonneau & Sellier (2011). It is possible that the actual bubble deformation exceeds that reported by Pigeonneau & Sellier (2011). Furthermore, due to the limitations in the azimuthal mesh size, the simulation can capture the evolution of the film up to  $t = 4.22$ , at which time the accumulated numerical round-off errors act to disturb the rim. Despite the limitations of the numerical tool, we can still capture the onset of the symmetry breaking event. Understanding the underlying physics that drives the symmetry breaking is the first step to understanding the subsequent rapid dimple discharge that affects the overall bubble lifetime. For the remainder of this paper, we focus on understanding the onset of symmetry breaking as shown in figures 2(b5) and 3(b).

Figure 4 provides the onset of symmetry breaking observed in the two-dimensional (2-D) simulation. At  $t = 4.10$ , the film thickness profile and the adsorbed surfactant distribution are both axisymmetric (figure 4a,d). The film thickness profile shows the presence of a dimple, which is the volume of liquid bounded by a ring of thin film at the rim,  $R = 0.88$ . The adsorbed surfactant concentration is depleted inside the dimple and approaches the initial adsorbed concentration of  $\Gamma_0/\Gamma_\infty$  for  $r > R$  (figure 4d). At  $t = 4.20$ , the effects of the instability are evident. Wrinkles in the rim location are observed in the film thickness contour plot (figure 4b). Fluctuations in the adsorbed surfactant concentration gradient in the radial direction can also be seen near  $r = 0.88$  in all azimuthal directions (figure 4e). Soon afterward, at  $t = 4.22$ , the rim wrinkling becomes even more pronounced, such that fluctuations in  $\hat{h}(t = 4.22, r = R, \theta)$  can easily be seen in figure 4(c). Correspondingly,  $\partial\Gamma^{(0)}/\partial r$  becomes more non-axisymmetric, with regions achieving a more dense surfactant packing than the initially adsorbed concentration (see the black regions in figure 4f). The topology presented in figure 4(c) is reminiscent of the interference pattern shown in figure 3(b). Due to the limitation in the numerical tool, the rest of the study is focused on examining the transition from an axisymmetric film to a non-axisymmetric film, as captured in figure 4 and figure 3(a,b).

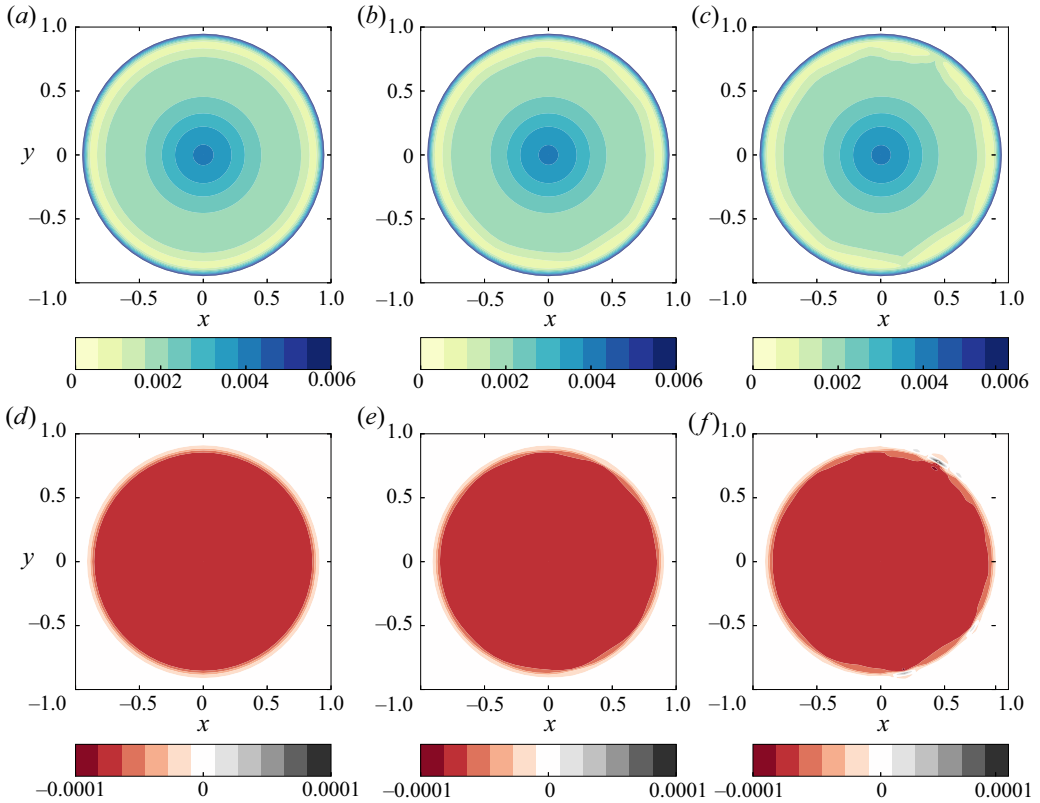


Figure 4. Film thickness ((a–c),  $\hat{h}$ ) and adsorbed surfactant concentration deviation from the initial concentration ((d,e),  $\Gamma^{(0)} - \Gamma_0/\Gamma_\infty$ ) during the symmetry breaking event observed in a 2-D numerical simulation ( $t = 4.10, 4.20, 4.22$ ). The simulation is conducted at  $\epsilon = 0.108$ ,  $t_{stop} = 3.11$ ,  $Ca = 1.2 \times 10^{-4}$ ,  $Bo = 0.021$ ,  $Ma = 7665$ ,  $Pe = 458$ ,  $Pe_S = 4580$ ,  $\Gamma_0/\Gamma_\infty = 0.938$ ,  $\alpha = 0.644$ ,  $\beta = 2.26$ ,  $La = 15.1$ . This parameter set corresponds to the experimental conditions described in figure 2. In this simulation the source of disturbance is the accumulated numerical error.

To further compare the evolution of the disturbance in the experiment and the simulation, we compare the Fourier transform of  $R$ ,

$$C_m = \frac{1}{2\pi} \int_{-\pi}^{\pi} e^{-im\theta} \frac{R(\theta) - R_{avg}}{R_{avg}} d\theta, \quad (4.1)$$

where  $m$  is the wavenumber and  $R_{avg}$  is the location of the rim averaged over all azimuthal directions. Figure 5(a) shows the magnitude of  $C_m$  deviation from  $C_m(t = 3.49)$  at selected time points during the symmetry breaking event in the experiment. The subtraction of  $|C_m(t = 3.49)|$  allows us to discard the signals associated with the pixelated nature of the interferograms and focus on the signals that grow over time as a result of disturbance growth. The experimental data shows that wavenumbers 9, 11, 13, 14 and 17 have significant disturbance growth. Among these wavenumbers,  $m = 11$  corresponds to the most prominent growth. In the corresponding 2-D simulation (figure 5b), wavenumbers 8 and 10 are the top two amplified modes. Despite the difference in the sources of disturbance for the experiment and the simulation, the rapid growth of modes associated with intermediate wavenumbers are observed. The good agreement

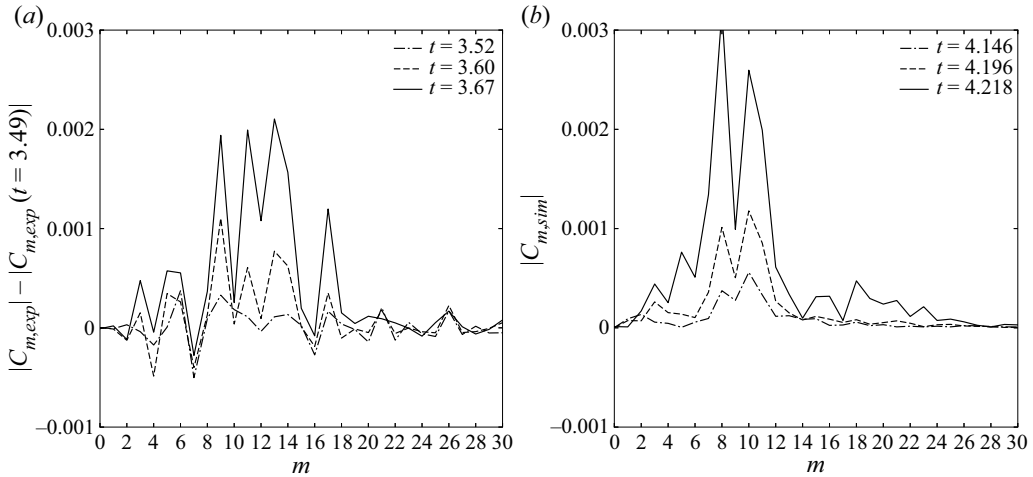


Figure 5. Fourier transform of the rim location during symmetry breaking for the experiment (a) and the simulation (b). The experimental condition and simulation parameters are described in figures 2 and 4.

between the experiment and the simulation gives us confidence in the ability of the theoretical model to capture the disturbance onset. To understand the symmetry breaking mechanism and the driving forces behind the mode selection, we therefore conduct a linear stability analysis.

#### 4.2. Linear stability analysis

In this section we examine the linear responses of the system subjected to a small perturbation. Experimental and simulation observations suggest that after the external forcing stops, the system soon succumbs to ambient disturbance and non-axisymmetric patterns with an intermediate wavenumber first developing around the rim of the film. To understand the system behaviour, we employ a linearized stability analysis.

The base state is the axisymmetric, one-dimensional (1-D) solution to the governing equations. Similar to our previous study (Shi *et al.* 2021), the base state evolves in time and in the radial direction. The linearized stability equations are derived by subtracting the axisymmetric, 1-D governing equations from the 2-D governing equations described in the theory section, followed by discarding all nonlinear terms in the disturbance quantities,  $\tilde{\psi}(t, r, \theta) \equiv \psi(t, r, \theta) - \psi_{1D}(t, r)$ , where  $\psi$  represents  $\hat{h}_1, \hat{P}, \langle \widehat{v_r} \rangle, \langle \widehat{v_\theta} \rangle, c^{(0)}$  and  $\Gamma^{(0)}$ . Based on the amplified perturbation in the experiment and in the simulation, we seek solutions in the form of  $\tilde{\psi} = \exp(im\theta)\bar{\psi}(t, r)$ , without making the usual assumption of exponential disturbance growth in time. After some algebra, we obtain the linearized governing equations for  $\bar{\psi}(t, r)$ .

The linearized disturbance equations associated with the mass and species balances are

$$\frac{\partial \bar{h}_1}{\partial t} + \frac{1}{r} \frac{\partial}{\partial r} (r (h_{1D} \overline{\langle v_r \rangle} + \bar{h}_1 \langle v_r \rangle_{1D})) + \frac{im}{r} h_{1D} \overline{\langle v_\theta \rangle} = 0, \quad (4.2)$$

$$\begin{aligned} & \frac{\partial \bar{c}}{\partial t} + \langle v_r \rangle_{1D} \frac{\partial \bar{c}}{\partial r} + \overline{\langle v_r \rangle} \frac{\partial c_{1D}}{\partial r} - \frac{1}{Pe} \left( \frac{1}{r} \frac{\partial}{\partial r} \left( r \frac{\partial \bar{c}}{\partial r} \right) - \frac{m^2}{r^2} \bar{c} \right) \\ & - \frac{1}{Pe} \frac{1}{h_{1D}} \left( \frac{\partial h_{1D}}{\partial r} \frac{\partial \bar{c}}{\partial r} + \frac{\partial \bar{h}_1}{\partial r} \frac{\partial c_{1D}}{\partial r} - \frac{\bar{h}_1}{h_{1D}} \frac{\partial h_{1D}}{\partial r} \frac{\partial c_{1D}}{\partial r} \right) \\ & = -\frac{2\alpha\beta}{h_{1D}} (\bar{c} - \bar{c}\Gamma_{1D} - c_{1D}\bar{\Gamma} - \bar{\Gamma}/La) + \frac{2\alpha\beta}{h_{1D}^2} \bar{h}_1 (c_{1D}(1 - \Gamma_{1D}) - \Gamma_{1D}/La) \end{aligned} \quad (4.3)$$

and

$$\begin{aligned} & \frac{\partial \bar{\Gamma}}{\partial t} + \frac{1}{r} \frac{\partial}{\partial r} (r\Gamma_{1D}^{(0)} \bar{v}_{r,s}) + \frac{1}{r} \frac{\partial}{\partial r} (r\bar{\Gamma} v_{r,s,1D}) + \frac{im}{r} \Gamma_{1D}^{(0)} \bar{v}_{\theta,s} \\ & - \frac{1}{Pe_s} \left( \frac{1}{r} \frac{\partial}{\partial r} \left( r \frac{\partial \bar{\Gamma}}{\partial r} \right) - \frac{m^2}{r^2} \bar{\Gamma} \right) = \alpha (\bar{c} - \bar{c}\Gamma_{1D}^{(0)} - c_{1D}^{(0)} \bar{\Gamma} - \bar{\Gamma}/La), \end{aligned} \quad (4.4)$$

where

$$\bar{v}_{r,s} = \overline{\langle v_r \rangle} - \frac{Ma}{6} \frac{\bar{h}_1}{1 - \Gamma_{1D}^{(0)}} \frac{\partial \Gamma_{1D}^{(0)}}{\partial r} - \frac{Ma}{6} \hat{h}_{1D} \left( \frac{1}{1 - \Gamma_{1D}^{(0)}} \frac{\partial \bar{\Gamma}}{\partial r} + \frac{\bar{\Gamma}}{(1 - \Gamma_{1D}^{(0)})^2} \frac{\partial \Gamma_{1D}^{(0)}}{\partial r} \right) \quad (4.5)$$

and

$$\bar{v}_{\theta,s} = \overline{\langle v_\theta \rangle} - \frac{Ma}{6} \frac{im}{r} \frac{\hat{h}_{1D}}{1 - \Gamma_{1D}^{(0)}} \bar{\Gamma}. \quad (4.6)$$

The linearized disturbance equations associated with the stress balances at the interfaces are

$$\begin{aligned} & \frac{1}{r} \frac{\partial}{\partial r} \left( r \frac{\partial \bar{h}_1}{\partial r} \right) - \frac{m^2}{r^2} \bar{h}_1 - B\bar{o}\bar{h}_1 + Ca\bar{P} + 2\epsilon Ca \frac{1}{r} \frac{\partial}{\partial r} (r\overline{\langle v_r \rangle}) + 2\epsilon Ca \frac{im}{r} \overline{\langle v_\theta \rangle} = 0, \quad (4.7) \\ & \frac{\partial \bar{P}}{\partial r} = \frac{2Ma}{\hat{h}_{1D}} \left( \frac{-1}{1 - \Gamma_{1D}^{(0)}} \frac{\partial \bar{\Gamma}}{\partial r} - \frac{\bar{\Gamma}}{(1 - \Gamma_{1D}^{(0)})^2} \frac{\partial \Gamma_{1D}^{(0)}}{\partial r} + \frac{\bar{h}_1}{\hat{h}_{1D}} \frac{1}{1 - \Gamma_{1D}^{(0)}} \frac{\partial \Gamma_{1D}^{(0)}}{\partial r} \right) \\ & + \epsilon \left( 2 \frac{\partial}{\partial r} \left( \frac{1}{r} \frac{\partial}{\partial r} (r\overline{\langle v_r \rangle}) \right) - \frac{m^2}{r^2} \overline{\langle v_r \rangle} + \frac{\partial}{\partial r} \left( \frac{im}{r} \overline{\langle v_\theta \rangle} \right) - \frac{2im}{r^2} \overline{\langle v_\theta \rangle} \right) \\ & + \epsilon \frac{2}{\hat{h}_{1D}} \frac{\partial \hat{h}_{1D}}{\partial r} \left( \frac{1}{r} \frac{\partial}{\partial r} (r\overline{\langle v_r \rangle}) + \frac{\partial \overline{\langle v_r \rangle}}{\partial r} + \frac{im}{r} \overline{\langle v_\theta \rangle} \right) \\ & + \epsilon \frac{2}{\hat{h}_{1D}} \left( \frac{1}{r} \frac{\partial}{\partial r} (r\langle v_r \rangle_{1D}) + \frac{\partial \langle v_r \rangle_{1D}}{\partial r} \right) \left( \frac{\partial \bar{h}_1}{\partial r} - \frac{\bar{h}_1}{\hat{h}_{1D}} \frac{\partial \hat{h}_{1D}}{\partial r} \right) \end{aligned} \quad (4.8)$$



and

$$\begin{aligned}
 \frac{im}{r} \bar{P} &= \frac{im}{r} \frac{2Ma}{\hat{h}_{1D}} \frac{-\bar{\Gamma}}{1 - \Gamma_{1D}^{(0)}} \\
 &+ \epsilon \left( -\frac{2m^2}{r^2} \langle v_\theta \rangle + \frac{\partial}{\partial r} \left( \frac{1}{r} \frac{\partial}{\partial r} (r \langle v_\theta \rangle) \right) + \frac{im}{r} \frac{1}{r} \frac{\partial}{\partial r} (r \langle v_r \rangle) + \frac{2im}{r^2} \langle v_r \rangle \right) \\
 &+ \epsilon \frac{im}{r} \frac{2}{\hat{h}_{1D}} \bar{h}_1 \left( \frac{1}{r} \frac{\partial}{\partial r} (r \langle v_r \rangle_{1D}) + \frac{\langle v_r \rangle_{1D}}{r} \right) \\
 &+ \epsilon \frac{1}{\hat{h}_{1D}} \frac{\partial \hat{h}_{1D}}{\partial r} \left( \frac{im}{r} \langle v_r \rangle + r \frac{\partial}{\partial r} \left( \frac{\langle v_\theta \rangle}{r} \right) \right). \tag{4.9}
 \end{aligned}$$

In the far field ( $r \rightarrow \infty$ ) these variables and their radial derivatives decay to zero.

The initial conditions for  $\bar{h}_1$ ,  $\bar{c}$  and  $\bar{\Gamma}$  are defined as

$$\bar{h}_1(t_{ini}, r) = \exp(-K(r - R)^2), \tag{4.10}$$

$$\bar{c}(t_{ini}, r) = \bar{\Gamma}(t_{ini}, r) = (r - R) \exp(-K(r - R)^2), \tag{4.11}$$

where  $K = 200$  and  $R$  represents the radial location where the film thickness is at its thinnest at  $t_{ini}$ , i.e. the rim. In other words, the disturbances are localized near the rim of the base state. These disturbances are smooth approximations of the difference between the fully 2-D simulations during disturbance onset and the corresponding 1-D base state. We assume that these disturbances act to promote the growth of the unstable mode. Choices of the exponential factor  $K$  have little effect on the subsequent analysis (figure 14). The initial conditions for  $\bar{P}$ ,  $\langle v_r \rangle$  and  $\langle v_\theta \rangle$  are obtained by solving (4.7), (4.8) and (4.9) simultaneously. By setting the wavenumber  $m$  to an integer and applying the initial and boundary conditions, we complete the initial value problem. These equations are time advanced numerically using the implicit time-stepping method.

Another way to study the system response to perturbation can be achieved by introducing perturbation of a known form and amplitude to the full 2-D simulation. By analysing the evolution of the injected perturbation in the linearized disturbance system and the full 2-D system, we can gain insight into the behaviour of the system. To such an end, the following perturbation is injected into the 2-D simulation at  $t_{ini}$ :

$$\psi_{inject} = C_{inject} \cos(m\theta) \bar{\psi}(t_{ini}, r). \tag{4.12}$$

Here  $\psi$  represents the six variables of interest and  $C_{inject} = 0.0001$  is a scaling factor to avoid numerical issues. The definitions for  $\bar{\psi}(t_{ini}, r)$  are given in (4.10) and (4.11).

Figure 6 shows the effects of a  $m = 10$  perturbation on a 2-D simulation. The perturbation is injected at  $t = 4$  and each column in the figure corresponds to a time point:  $t = 4, 4.005$  and  $4.1$ . Upon perturbation injection, features associated with the wavenumber of the injected perturbation become immediately apparent. For  $\hat{h}$  and  $\Gamma^{(0)} - \Gamma_0/\Gamma_\infty$ , the disturbance grows with time, leading to more pronounced rim wrinkling and fluctuations in  $\partial \Gamma^{(0)}/\partial r$  (figure 6a-f). Here  $\langle \hat{v}_r \rangle$  and  $\langle \hat{v}_\theta \rangle$  first decrease in amplitude, but grow at later times. The signs of  $\langle \hat{v}_r \rangle$  and  $\langle \hat{v}_\theta \rangle$  give a clear indication of the flow directions. A positive value in  $\langle \hat{v}_r \rangle$  corresponds to radial flow from the dimple into the bulk, and a positive value in  $\langle \hat{v}_\theta \rangle$  corresponds to counterclockwise flow in the azimuthal direction. In each  $2\pi/m$  azimuthal segment there is a pair of locally circulating flows clustered around the rim.

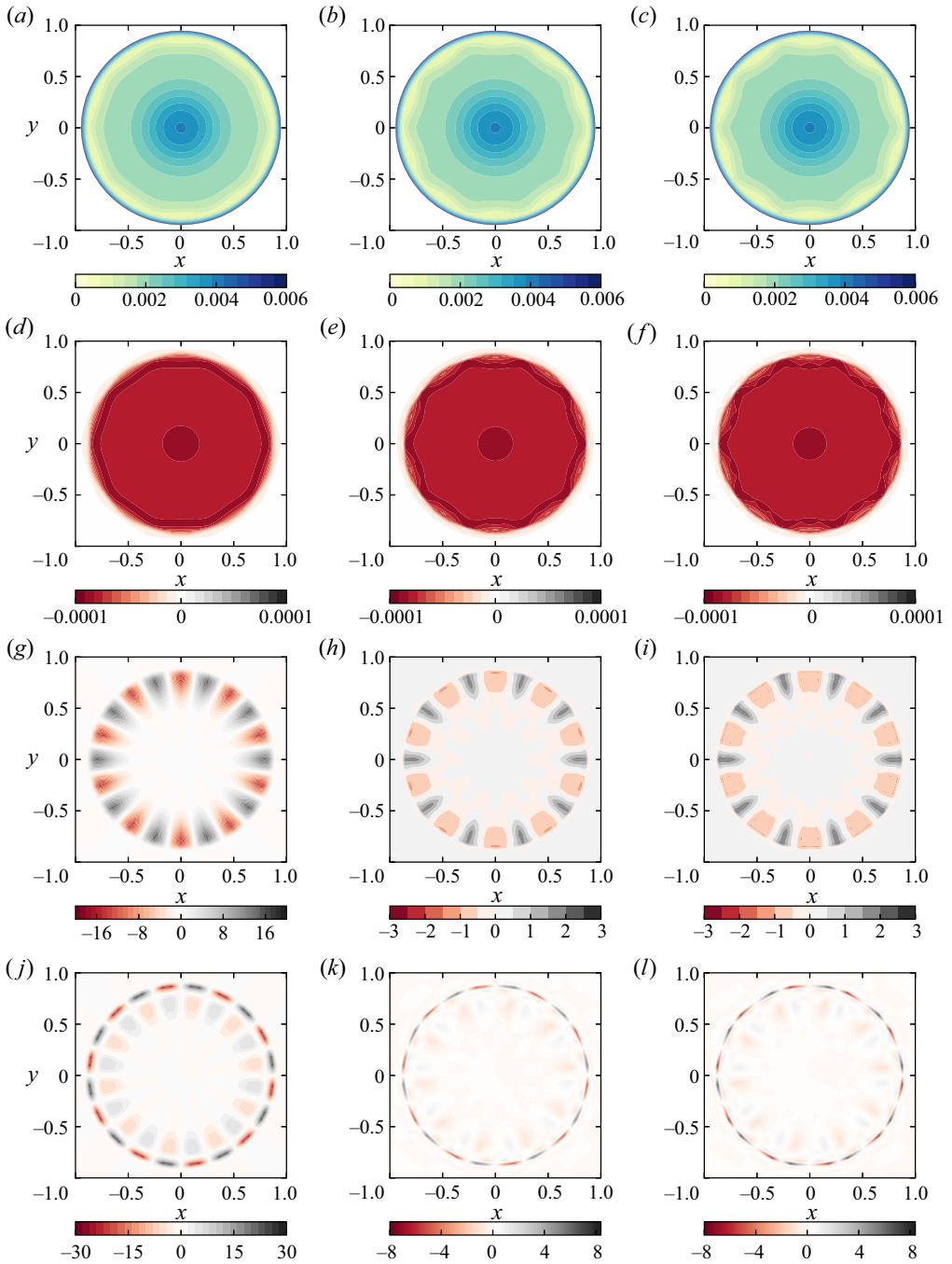


Figure 6. Responses of the 2-D simulation to  $m = 10$  perturbation injection at  $t = 4$  for selected variables:  $\hat{h}$  (a-c),  $\Gamma^{(0)} - \Gamma/\Gamma_\infty$  (d-f),  $\langle \hat{v}_r \rangle$  (g-i) and  $\langle \hat{v}_\theta \rangle$  (j-l). Plots (a,d,g,j) are plotted at  $t = 4$ , the time of perturbation injection. Plots (b,e,h,k) are plotted at  $t = 4.005$  and plots (c,f,i,l) are plotted at  $t = 4.01$ . The simulation parameters are the same as those described in figure 4.

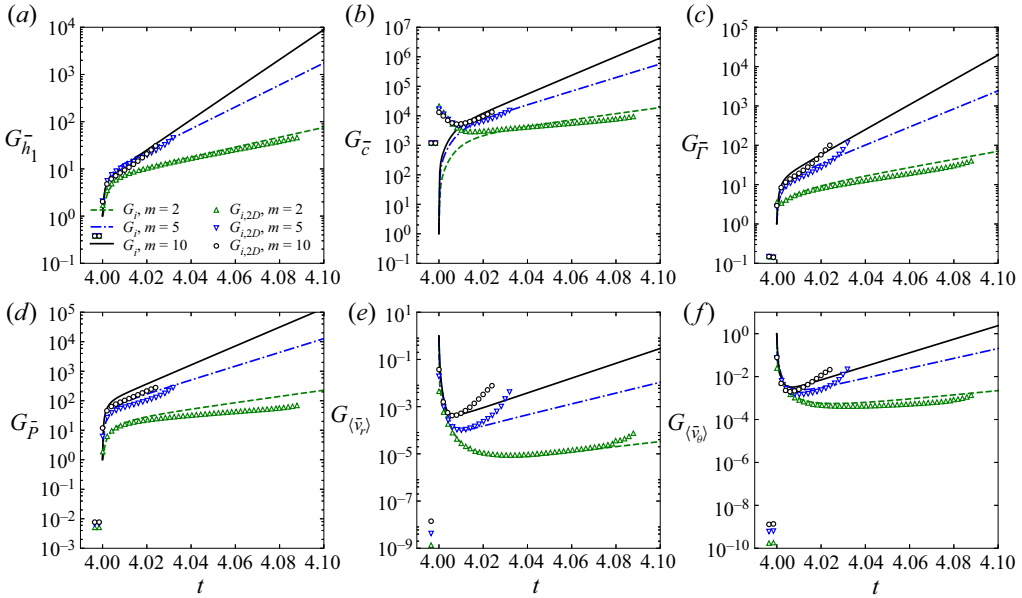


Figure 7. Comparison of gains of the linearized disturbance quantities (lines) and gains of the injected disturbances in the 2-D simulations (symbols) for three different wavenumbers. The simulation parameters are the same as those described in figure 4.

To measure the growth of these disturbance quantities, we introduce the ‘gain’ for each variable. i.e.

$$G_{\bar{\psi}}(t) = \frac{\int_0^\infty \bar{\psi}^2 r \, dr}{\int_0^\infty \bar{\psi}_{ini}^2 r \, dr}. \tag{4.13}$$

If the value of  $G_{\bar{\psi}}(t)$  increases above unity, then the corresponding disturbance is growing, indicative of an unstable system. Similarly, the gain associated with the perturbation injected into the 2-D simulation is

$$G_{\psi,2D}(t) = \frac{\int_0^{2\pi} \int_0^2 (\psi - \psi_{1D})^2 r \, dr \, d\theta}{\int_0^{2\pi} \int_0^2 \psi_{inject}^2 r \, dr \, d\theta}. \tag{4.14}$$

The upper integration bound in the radial direction for  $G_{\psi,2D}$  is at  $r = 2 > R$ . This truncation is necessary to exclude the effects of the accumulated solution difference between the 2-D simulation and the corresponding 1-D base state prior to  $t_{ini}$ . Because the disturbances introduced to the system are localized to the rim, this truncation still accounts for the changes to the variable as a result of perturbation injection.

Figure 7 shows the comparison in the evolution of  $G_{\bar{\psi}}$  and  $G_{\psi,2D}$ , for all six disturbance quantities and at three wavenumbers,  $m = 2, 5, 10$ . Disturbance is injected into the 2-D simulation at  $t_{ini} = 4$  and the linearized disturbance equations are time advanced starting at  $t_{ini} = 4$ . Here  $G_{\psi,2D}$  is plotted up to the point where azimuthal resolution is lost.

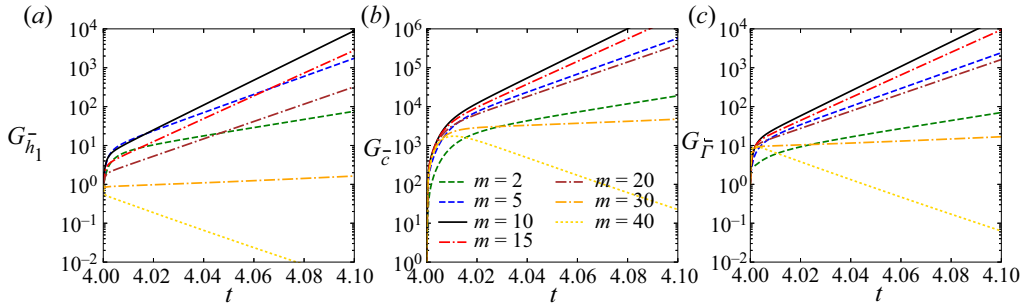


Figure 8. Evolution of the linearized disturbance quantities at different wavenumbers. The simulation parameters are the same as those described in figure 7. For this set of parameters, the wavenumber that maximizes disturbance growth is  $m = 10$ .

The growth in  $G_{\bar{\psi}}$  and  $G_{\psi,2D}$  shows good agreement for all variables except for  $\bar{c}$ . The good agreement in  $G_{\bar{\psi}}$  and  $G_{\psi,2D}$  verifies that the perturbation injection in both approaches are implemented correctly. Furthermore, it indicates that the system responds linearly in the short time period after the perturbation injection. The discrepancy in  $\bar{c}$  is caused by a significant difference between  $c^{(0)}$  and  $c_{1D}^{(0)}$  at the time of perturbation injection. The significance of the difference is reflected in the large value of  $G_{c,2D}$  prior to  $t_{ini} = 4$ . Despite the discrepancy at the onset of the disturbance injection, the eventual growth rate in  $G_{\bar{c}}$  and  $G_{c,2D}$  still show good agreement, further indicating that the system responds linearly to the small disturbance.

We find that  $G_{\bar{\psi}}$  and  $G_{\psi,2D}$  for all three wavenumbers show eventual growth after the introduction of disturbance, indicating that the system is unstable. For the three wavenumbers probed in this figure, in general,  $m = 10$  shows the fastest growth rate and  $m = 2$  has the slowest growth rate. For  $\bar{h}_1$ , during  $t_{ini} < t < t_{ini} + 0.01$ , the growth rate for  $m = 5$  is faster than  $m = 10$ . After  $t = t_{ini} + 0.01$ ,  $G_{\bar{h}_1}$ ,  $m = 10$  is larger than  $G_{\bar{h}_1}$ ,  $m = 5$ . This growth rate crossover is also captured by disturbance injection into the 2-D equations. This crossover is only observed in  $\bar{h}_1$ , which may explain why there are multiple fast growing wavenumbers associated with the change in the rim location observed both in the experiment and the simulation presented in the previous section. These observations call for a refined sweep in the wavenumber.

Figure 8 shows the evolution in the gain from  $t_{ini} = 4$  to  $t = 4.1$  for  $\bar{h}_1$ ,  $\bar{c}$  and  $\bar{r}$  at a variety of wavenumbers, ranging from 2 to 40. All simulation parameters are the same as those used in figure 7. For this parameter set,  $m = 10$  corresponds to the fastest disturbance growth. As the wavenumber increases, the growth rate in the gain for all three variables is reduced. When the wavenumber is increased to  $m = 40$ , the value of the gain eventually decays below unity, indicating that the system is linearly stable to high wavenumber perturbations.

### 4.3. Symmetry breaking mechanism

We are now in a position to understand the underlying physical mechanism that drives this instability. The form of the linearized disturbance equations prohibits explicit expressions of  $\bar{P}$ ,  $\langle v_r \rangle$  and  $\langle v_\theta \rangle$ , in terms of capillarity, Marangoni and gravity contributions. The best we can do is to examine the combined effects of those physical forces on  $\langle v_r \rangle$  and  $\langle v_\theta \rangle$  and

see how these two terms affect the time rate of change of  $G_{\bar{h}_1}$  and  $G_{\bar{\Gamma}}$ . Because  $\bar{c}$  is closely associated with  $\bar{\Gamma}$ , we shall only examine  $\bar{\Gamma}$  to avoid redundancy.

Rearranging (4.2), yields

$$\frac{1}{2} \frac{dG_{\bar{h}_1}}{dt} = A_{v_r} + A_{v_\theta}, \tag{4.15}$$

where

$$A_{v_r} = - \frac{\int_0^\infty \bar{h}_1 \frac{1}{r} \frac{\partial}{\partial r} (r \hat{h}_{1D} \overline{\langle v_r \rangle}) r \, dr}{\int_0^\infty \bar{h}_{1,ini}^2 r \, dr} - \frac{\int_0^\infty \bar{h}_1 \frac{1}{r} \frac{\partial}{\partial r} (r \bar{h}_1 \widehat{\langle v_r \rangle}_{1D}) r \, dr}{\int_0^\infty \bar{h}_{1,ini}^2 r \, dr} \tag{4.16}$$

and

$$A_{v_\theta} = - \frac{\int_0^\infty \bar{h}_1 \hat{h}_{1D} \frac{im \overline{\langle v_\theta \rangle}}{r} r \, dr}{\int_0^\infty \bar{h}_{1,ini}^2 r \, dr}. \tag{4.17}$$

Similarly, (4.4) can be rearranged into

$$\frac{1}{2} \frac{dG_{\bar{\Gamma}}}{dt} = B_{v_r} + B_{v_\theta} + B_{Diff} + B_{Ads}, \tag{4.18}$$

where

$$B_{v_r} = - \frac{\int_0^\infty \bar{\Gamma} \frac{1}{r} \frac{\partial}{\partial r} (r \Gamma_{1D}^{(0)} \bar{v}_{r,s}) r \, dr}{\int_0^\infty \bar{\Gamma}_{ini}^2 r \, dr} - \frac{\int_0^\infty \bar{\Gamma} \frac{1}{r} \frac{\partial}{\partial r} (r \bar{\Gamma} v_{r,s,1D}) r \, dr}{\int_0^\infty \bar{\Gamma}_{ini}^2 r \, dr}, \tag{4.19}$$

$$B_{v_\theta} = - \frac{\int_0^\infty \bar{\Gamma} \Gamma_{1D}^{(0)} \frac{im \bar{v}_{\theta,s}}{r} r \, dr}{\int_0^\infty \bar{\Gamma}_{ini}^2 r \, dr}, \tag{4.20}$$

$$B_{Diff} = - \frac{1}{Pe_S} \frac{\int_0^\infty \bar{\Gamma} \left( \frac{1}{r} \frac{\partial}{\partial r} \left( r \frac{\partial \bar{\Gamma}}{\partial r} \right) - \frac{m^2}{r^2} \bar{\Gamma} \right) r \, dr}{\int_0^\infty \bar{\Gamma}_{ini}^2 r \, dr} \tag{4.21}$$

and

$$B_{Ads} = \alpha \frac{\int_0^\infty \bar{\Gamma} \bar{c} (1 - \Gamma_{1D}^{(0)}) r \, dr}{\int_0^\infty \bar{\Gamma}_{ini}^2 r \, dr} - \alpha \frac{\int_0^\infty \bar{\Gamma}^2 (c_{1D}^{(0)} + 1/La) r \, dr}{\int_0^\infty \bar{\Gamma}_{ini}^2 r \, dr}. \tag{4.22}$$

With the above definition, we can observe the overall effects of radial advection ( $A_{v_r}$  and  $B_{v_r}$ ), azimuthal advection ( $A_{v_\theta}$  and  $B_{v_\theta}$ ), diffusion ( $B_{Diff}$ ) and adsorption ( $B_{Ads}$ ) on the time rate of change of  $G_{\bar{h}_1}$  and  $G_{\bar{\Gamma}}$ . For each of these quantities, a positive value means disturbance growth and a negative value corresponds to stabilizing effects. **Figure 9** shows the evolution of  $dG_{\bar{h}_1}/dt$ ,  $dG_{\bar{\Gamma}}/dt$  and the associated physical contributing terms at

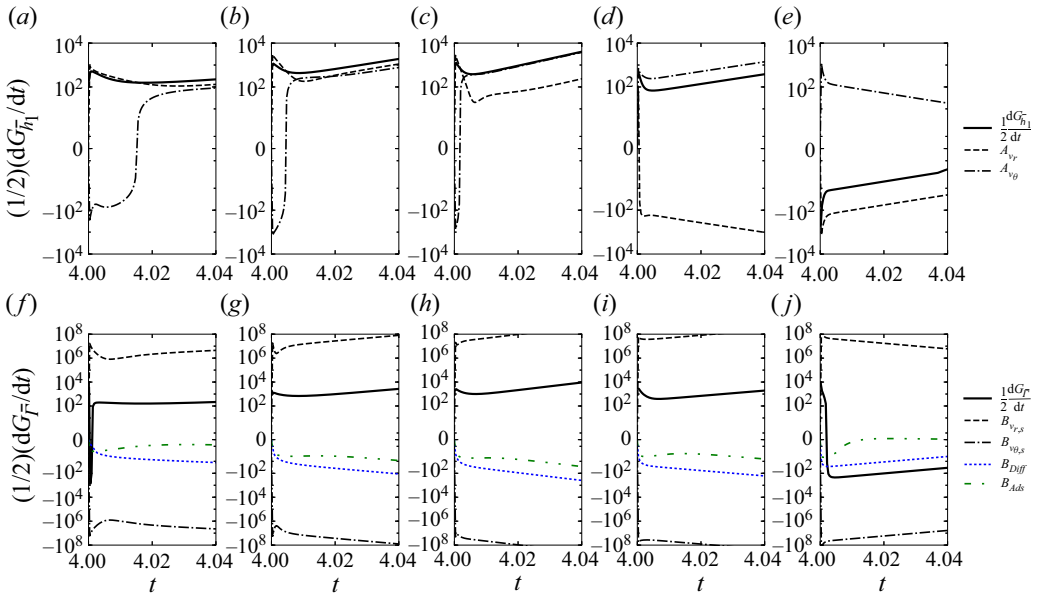


Figure 9. Evolution of the time rate of change in the gain for  $\bar{h}_1$  (a–e) and  $\bar{\Gamma}$  (f–j) and contributing physical forces for five wavenumbers. From left to right, each column corresponds to one wavenumber  $m = 2, 5, 10, 20, 40$ , respectively. The simulation parameters are the same as those described in figure 8.

five different wavenumbers:  $m = 2, 5, 10, 20, 40$ . The simulation conditions are the same as in figure 8. The y-axis scale in figure 9 is a symmetric log plot, where large absolute values are plotted on a log scale and values near zero are plotted on a linear scale.

For  $m = 2, 5, 10$ ,  $\bar{h}_1$  (figure 9a–c) and  $\bar{\Gamma}$  (figure 9f–h) grow over time, as evidenced by the positive values of  $dG_{\bar{h}_1}/dt$  and  $dG_{\bar{\Gamma}}/dt$ . For a short time period after  $t_{ini} = 4$ ,  $A_{v_r}$  is the dominant factor in destabilizing  $\bar{h}_1$  and  $A_{v_\theta}$  is briefly stabilizing. As time goes on,  $A_{v_\theta}$  increases in magnitude and becomes the dominant cause for destabilization in  $\bar{h}_1$ . For  $\bar{\Gamma}$ ,  $B_{v_r,s}$  acts to destabilize the system, while  $B_{v_\theta,s}$  acts to stabilize. The balance in these two terms determine the overall growth rate, which increases as the wavenumber increases from 2 to 10. The contributions from diffusion and surfactant adsorption terms have negligible stabilizing effects.

The term  $m = 20$  marks a transition point in the behaviour of the disturbance growth rate (figure 9d,i).  $A_{v_r}$  becomes stabilizing and its stabilizing influence on  $\bar{h}_1$  reduces the growth rate of  $G_{\bar{h}_1}$  when compared with  $dG_{\bar{h}_1}/dt$  for  $m = 10$ . Correspondingly, the magnitudes of  $B_{v_r,s}$  and  $B_{v_\theta,s}$  decrease, leading to a decrease in the growth rate of  $dG_{\bar{\Gamma}}/dt$  at  $m = 20$ . At  $m = 40$ , the system is linearly stable (figure 9e,j). Both  $dG_{\bar{h}_1}/dt$  and  $dG_{\bar{\Gamma}}/dt$  become negative as a result of reduction in the amplitudes of  $A_{v_r}$ ,  $A_{v_\theta}$ ,  $B_{v_r}$  and  $B_{v_\theta}$ . The variations in the amplitudes of these four terms lead to the change in disturbance growth rates observed in figure 8 and are the reasons behind wavenumber selection.

Figure 10 shows the comparisons of the base state variables and selected radial cuts of variables in the 2-D simulation with  $m = 10$  disturbance injection. Here  $\theta = 0$  and  $\theta = \pi/m$  are chosen because they correspond to the first half-period in the injected disturbance (see (4.12)). Figure 10(a) shows the base state film thickness at  $t = 4.005$  (black solid line). In contrast,  $\hat{h}(\theta = 0)$  (red dashed line) shows an increase in film thickness relative to the base state and  $\hat{h}(\theta = \pi/m)$  (blue dash-dotted line) shows film thinning relative to the



## Instability of surfactant films

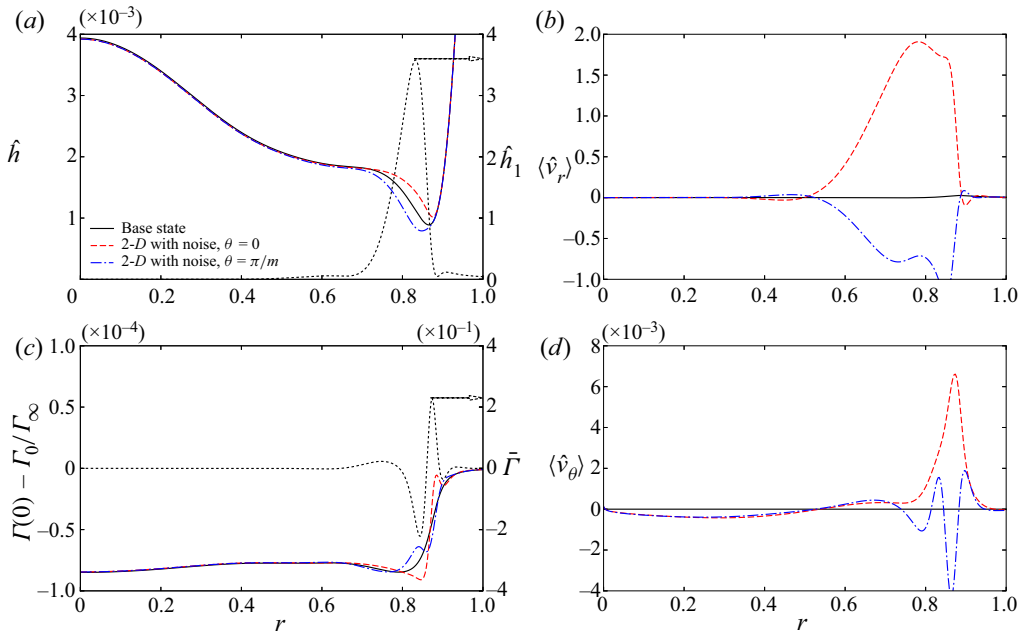


Figure 10. Comparisons of the radial profile evolution between the base state quantities (black solid lines) and the  $\theta = 0$  (red dashed lines) and  $\theta = \pi/m$  (blue dash-dotted lines) cuts in the 2-D simulation with  $m = 10$  disturbance injection at  $t = 4$ . Plots (a,c) also show the linearized disturbance quantities,  $\bar{h}_1$  and  $\bar{\Gamma}$ , plotted on the right y axis in black dotted lines. The linearized disturbance equations are solved with  $m = 10$ ,  $t_{ini} = 4$ . All quantities are plotted at  $t = 4.005$ . The other simulation parameters are the same as those described in figure 7.

base state. The linearized disturbance in film thickness ( $\bar{h}_1$ , black dotted line) shows the change in film thickness is concentrated near the rim. Figure 10(b) shows depth-averaged velocity in the radial direction. A positive value indicates flow away from  $r = 0$ . The base state  $\langle \hat{v}_r \rangle$  indicates that liquid is leaving the dimple region at a relatively slow rate, when compared with the 2-D simulation with disturbance injection. In the direction where the disturbance acts to thicken the film,  $\langle \hat{v}_r \rangle$  ( $\theta = 0$ ) flows out of the dimple region at a fast rate, whereas  $\langle \hat{v}_r \rangle$  ( $\theta = \pi/m$ ) indicates liquid is being drawn back towards  $r = 0$ . As a result, surfactants in the  $\theta = 0$  and  $\theta = \pi/m$  directions are convected in opposite radial directions (figure 10c). In  $\theta = 0$ , when compared with the base state, the surface adsorbed surfactant concentration is depleted in the region shortly before the rim and enriched over  $r > R$ . This trend is also observed in the radial profile of the linearized disturbance quantity,  $\bar{\Gamma}$ . In contrast,  $\Gamma^{(0)}(\theta = \pi/m) - \Gamma_0/\Gamma_\infty$  is enriched over  $0.8 < r < R$  when compared with  $\Gamma_{1D}^{(0)} - \Gamma_0/\Gamma_\infty$ . Thus, an azimuthal surfactant concentration gradient is established, such that the Marangoni stress will draw liquid from  $\theta = \pi/m$  toward  $\theta = 0$  over  $0.8 < r < R$ . This clockwise flow is reflected in the negative valued  $\langle \hat{v}_\theta \rangle$  ( $\theta = \pi/m$ ) around  $r = R$  (figure 10(d) blue dash-dotted line). In other words, liquid is flowing from the disturbance-thinned region into the already thickened film region. Here  $\langle \hat{v}_\theta \rangle$  ( $\theta = 0$ ) is largely positive, indicating a counterclockwise flow that is driven both by liquid mass conservation and the enriched surface adsorbed surfactant in the region just beyond the rim.

Combining the observations made in figures 6 and 9, we can begin to understand the underlying physical mechanism. An azimuthal direction fluctuation in film thickness

leads to local fluctuations in  $\langle \hat{v}_r \rangle$ . A locally thickened film acts to dispel liquid from the dimple, leading to an increase in  $\langle \hat{v}_r \rangle$ . Conversely, a locally thinned film leads to liquid mass retracting into the dimple region, resulting in  $\langle \hat{v}_r \rangle$  flowing towards  $r = 0$ . The difference in the flow directions convects the surface adsorbed surfactants in different radial directions. This process creates an azimuthal surfactant gradient that draws liquid from the already relatively thin region into the disturbance-enriched thick film region. As a result of these combined flow motions, the initially thickened film thickens further, leading to the observed flow instability.

#### 4.4. The most dangerous wavenumber

In this section we study the effect of  $t_{stop}$  on the maximum growth wavenumber,  $m_{max}$ , in an attempt to elucidate the factors that control  $m_{max}$ . For context, the equilibrium  $t_{stop,eqlb}$  can be approximated by balancing the buoyancy force to the capillary force,  $\rho g \frac{4}{3} \pi a^3 = \gamma_{solution} 2\pi R_{eqlb}$ , where  $\gamma_{solution}$  is the surface tension of the surfactant solution and  $R_{eqlb}$  is the approximate rim location at equilibrium for a spherical bubble. After some simple computation, one can obtain  $t_{stop,eqlb} = 1.14$  for this system. We now conduct a study to understand the underlying mechanisms that determine  $m_{max}$ , by perturbing  $t_{stop}$  beyond its equilibrium value.

First, we observe the effect of increasing  $t_{stop}$  on the base state, by solving the axisymmetric, 1-D governing equations with all parameter values presented in [table 1](#). [Figures 11\(a\)](#) and [11\(b\)](#) show the radial profiles of film thickness ( $\hat{h}_{1D}$ ) and surface concentration deviation from its initial value ( $\Gamma_{1D}^{(0)} - \Gamma_0/\Gamma_\infty$ ), plotted at  $t = t_{stop} + 1$  for seven different  $t_{stop}$  values. The figures are plotted at  $t = t_{stop} + 1$  because they are the initial time used in evolving the linearized stability equations subsequently. The protrusion of the air bubble above the initially flat liquid–air interface grows with increasing values of  $t_{stop}$ . As a result, the location of the rim,  $R$ , moves further away from the centreline, thereby widening the circumferential domain over which the disturbance can travel in the azimuthal direction. Similarly, an increase in  $t_{stop}$  shifts the location of the surfactant gradient radially outward ([figure 11b](#)).

[Figure 11\(c\)](#) shows the corresponding pressure profiles as the blue solid lines. In all seven cases, the pressure at the apex of the bubble is higher than in the bulk. The pressure drop occurs over the location of the rim. The dominant flow driving forces in the radial direction are the pressure gradient,  $\partial \hat{P}_{1D} / \partial r$ , and the Marangoni stresses,  $-(2Ma/\hat{h}_{1D}(1 - \Gamma_{1D}^{(0)}))(\partial \Gamma_{1D}^{(0)} / \partial r)$ . The difference in these two quantities dictate the overall flow direction. [Figure 11\(d\)](#) shows that, for the seven conditions examined,  $\partial \hat{P}_{1D} / \partial r$  overwhelms the Marangoni stresses, leading to liquid discharge from the dimple into the bulk region. Furthermore, we define  $\Delta R$  to be the radial width over which the amplitude in the difference of the pressure gradient and the Marangoni driving forces is appreciable,

$$Ca \frac{\partial \hat{P}_{1D}}{\partial r} + \frac{2MaCa}{\hat{h}_{1D}(1 - \Gamma_{1D}^{(0)})} \frac{\partial \Gamma_{1D}^{(0)}}{\partial r} < -0.0001. \tag{4.23}$$

With a good understanding of the effects of  $t_{stop}$  on the base state, we now probe its effect on the growth rate of the disturbance variables. For each of the  $t_{stop}$  values presented in [figure 11](#), we solved the linearized disturbance equations at  $t_{ini} = t_{stop} + 1$ . [Figures 12\(a\)](#) and [12\(b\)](#) show the value of gain for  $\bar{h}_1$  and  $\bar{\Gamma}$  plotted at  $t = t_{ini} + 0.1$  for

## Instability of surfactant films

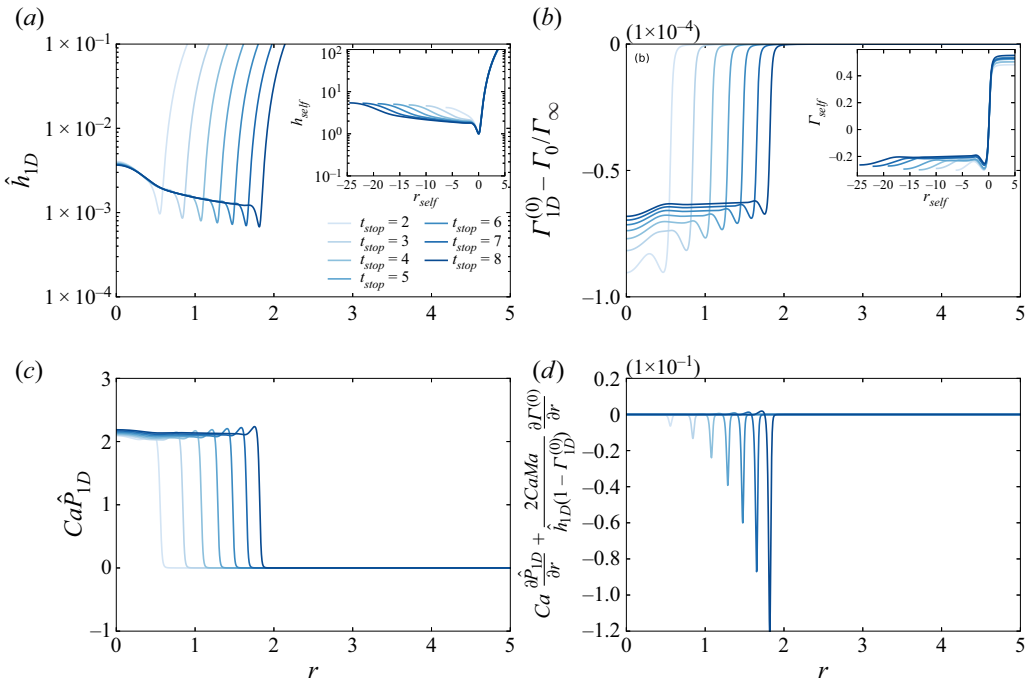


Figure 11. Effects of  $t_{stop}$  on selected base state variables: (a) film thickness, (b) surface adsorbed surfactant concentration deviation from its initial value, (c) pressure and (d) the difference between the pressure gradient and the Marangoni stresses. The inset figures in (a,b) are the rescaled film thickness and surface adsorbed surfactant concentration, where  $r_{self} = (r - R) / (\hat{h}_{1D,R}^2 / (\partial \Gamma_{1D}^{(0)} / \partial r|_R))^{1/3}$ ,  $h_{self} = \hat{h}_{1D} / \hat{h}_{1D}(r = R)$  and  $\Gamma_{self} = (\Gamma_{1D}^{(0)} - \Gamma_{1D}^{(0)}(r = R)) / (\hat{h}_{1D,R} (\partial \Gamma_{1D}^{(0)} / \partial r|_R))^{2/3}$ . The variables exhibit self-similar behaviour. All the radial profiles are plotted at  $t = t_{stop} + 1$ . The simulation parameters are provided in table 1.

a range of wavenumbers. It is clear from these two sets of dispersion curves that there is a wavenumber that corresponds to the maximum growth rate for each  $t_{stop}$ , and the maximum growth rate wavenumber ( $m_{max}$ ) increases monotonically with  $t_{stop}$ . Combining observations made on figure 11, we now plot  $m_{max}$  against  $R(t_{ini}) / \Delta R$  (figure 12c), which is the ratio of the rim radius at the time of disturbance injection to the width of pronounced pressure gradient contribution from capillarity and Marangoni forces. Figure 12(c) shows a clear linear relationship between the two quantities. In fact,  $m_{max} \sim 2R / \Delta R$ .

Figure 13 provides a comparison between the most dangerous wavenumbers obtained in the linear stability analysis and those of the experiments. Because the interferograms only give film thickness information and not the distribution of surfactant species, it is impossible to obtain the equivalent value of  $\Delta R$  in the experiments. Therefore, the effect of  $t_{stop}$  on  $m_{max}$  is examined. The linear stability analysis data indicates that  $m_{max}$  monotonically increases with  $t_{stop}$ , confirming the observations made in figure 12. Two sets of experimental data are presented in figure 13. For the experiment with  $t_{stop} = 3.11$ , the wavenumbers with the fastest growth rates are  $m = 11$  and  $m = 13$ , consistent with figure 5(a). Experiment 2 has a smaller  $t_{stop} = 2.33$  and its most dangerous wavenumbers are  $m = 8$  and  $m = 10$ . The trend in the two sets of experiments suggests that  $m_{max}$  grows with increasing values of  $t_{stop}$ . The offset in  $m_{max}$  between the experimental data and the linear stability analysis can be the result of the non-deformability assumption applied to the bubble interface in the model and measurement errors associated with the pixelated

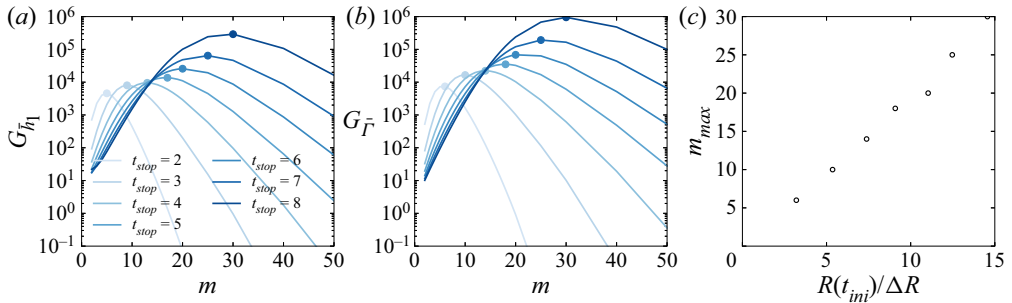


Figure 12. (a,b) Gain as a function of wavenumber for linearized disturbance quantities  $\bar{h}_1$  and  $\bar{F}$ . Each linearized stability simulation starts at  $t_{ini} = t_{stop} + 1$  and the value of the gain is plotted at  $t = t_{ini} + 0.1$ . The dot on each line signifies the maximum growth wavenumber,  $m_{max}$ . (c) Linear dependence of  $m_{max}$  on the ratio of rim location at disturbance injection time ( $R$ ) to the width of pronounced radial direction pressure gradient ( $\Delta R$ ). The simulation parameters are provided in table 1.

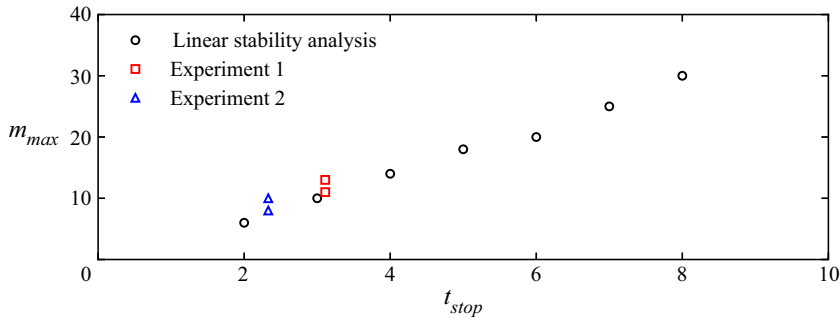


Figure 13. Comparison of  $m_{max}$  obtained from linear stability analysis (circles) and from experiments (triangles and squares). The experimental conditions for experiment 1 correspond to the values in table 1 with  $t_{stop} = 3.11$ . The experimental conditions for experiment 2 are as follows:  $\epsilon = 0.137$ ,  $t_{stop} = 2.33$ ,  $Ca = 7.34 \times 10^{-5}$ ,  $Bo = 0.029$ ,  $Ma = 9700$ ,  $Pe = 482$ ,  $Pe_S = 4820$ ,  $\Gamma_0/\Gamma_\infty = 0.938$ ,  $\alpha = 0.86$ ,  $\beta = 1.70$ ,  $La = 15.1$ .

nature of the images captured by the top camera. Despite the difference in the values, the experimental  $m_{max}$  values fall within the range of  $m_{max}$  obtained in the simulation. The agreement in  $m_{max}$  and the trend with respect to  $t_{stop}$  provide some validation for the linearized stability analysis. The Fourier transform of the rim location for experiment 2 can be found in the Appendix (figure 15).

#### 4.5. Comparison with surfactant spreading and marginal regeneration

The behaviour of our system is reminiscent of the fingering behaviour associated with the deposition of a surfactant droplet onto a thin liquid film (Warner, Craster & Matar 2004). We shall refer to their study as WCM henceforth. In the WCM system, a droplet of soluble surfactant is deposited on an initially surfactant free thin liquid film. The deposited droplet spreads and the surfactant advances from the droplet to surfactant-poor regions on the thin liquid film, driven by Marangoni stresses. As the leading front spreads radially outward, a severely thinned region of the film is formed between the deposited drop and the leading front. This thin region is effectively pinning the droplet in place and delaying the mass transport. Experimental observations show that this flow process is susceptible

to ambient disturbances, and fingering patterns can be observed forming in the pinning region, where the film is at its thinnest (see figure 1 in WCM). The base state for the WCM system is the streamwise spreading process and the effect of disturbance in the transverse direction is studied. Their linear stability analysis reveals that, for a given set of parameters, there is a maximally amplified intermediate wavenumber associated with the transverse disturbance. This disturbance is trapped in the pinning region, rather than at the advancing front. The physical mechanism behind the growth of the disturbance can be summarized as follows: a small fluctuation in film thickness leads to a local increase in film thickness and subsequently the local surface velocity, which scales with film thickness. The increase in local surface velocity leads to enhanced advection of surfactant away from this thick film region, thereby increasing the surface tension locally. Marangoni stress draws more liquid into this locally thick, high surface tension region, contributing to the growth of the disturbance.

The instability in this study shares many common features with the surfactant spreading system. In both systems, the disturbances are amplified in the region where the liquid film is at its minimum thickness, i.e. the pinning region that restricts flow. Disturbances act to locally thicken the surfactant film (figure 7*a* in WCM and figure 10*a*). Simultaneously, the surface adsorbed surfactant concentration is depleted in the thinning region and enriched just beyond the rim (figure 7*b* in WCM and figure 10*d*). The perturbation in the surfactant concentration leads to Marangoni flows in the transverse direction that further act to increase the thickness in the already thickened film. Both systems exhibit mode selection behaviour (figure 6 in WCM and figure 8), with an intermediate wavenumber that gives the fastest growth rate. Jensen & Naire (2006) conducted an extension study on the WCM system and found that self-similar structures can be determined in different regions of the spreading event by appropriately rescaling the film thickness profiles and the concentration profiles. By using the scales provided in (Jensen & Naire 2006), we found self-similar features in the base state solution (insets in figure 11*a,b*). More importantly, Jensen & Naire (2006) found that, for the WCM system, the wavelength of most dangerous linearized disturbance is comparable to the width of the pinning region. This relationship confirms our observation of  $m \sim R/\Delta R$ .

These two systems also have features that are unique. The dominant flow driving forces are different in the two studies: the initially deposited surfactant droplet creates the surface tension gradient that drives the spreading event in the WCM study, whereas in our system, external forcing creates the surfactant gradient through advection, yielding a high surface tension region over the apex of the bubble and a low surface tension region in the bulk. Thus, the surface tension gradient in the streamwise direction for the two systems are reversed. In our system, after  $t_{stop}$ , the radial pressure gradient overwhelms Marangoni flow and acts to expel the liquid from the dimple (figure 11*d*), leading to the sustained decrease in maximum film thickness observed in figure 2(*a*) and figure 5 of Frostad *et al.* (2016). The geometry of the substrates affects the formulation of the lubrication theory: in the WCM study the lower surface is a flat wall with a no-slip boundary condition; in this study the lower surface is an air bubble whose interfacial tension is dependent on the soluble surfactant adsorption kinetics. Finally, the curvature of the substrates affect the subsequent flow development. In the WCM study the deposited surfactant droplet expands indefinitely into domains that are covered by a clean liquid film of constant thickness. As a result, the fingers obtain significant growth (figure 14 in WCM). In contrast, in this study the curvature of the air bubble creates a domain with drastic film thickness increase beyond the rim in the radial direction (figure 10*a*). When perturbation disturbs the film thickness, the liquid in the dimple flows through the path of least resistance and discharges into the bulk region. In other words, the curvature of the lower surface limits the spatial domain

over which disturbances can grow and, as a result, no pronounced fingering effects are observed in this study.

Finally, some discussion is in order to compare this study to the marginal regeneration phenomenon. Figure 1 of Miguët *et al.* (2021) shows a typical marginal regeneration process developed over a freely suspended air bubble in a surfactant solution. The thin liquid film and the bulk of the surfactant solution is separated by a rim with minimum film thickness (see figure 6 of Lhuissier & Villermaux 2012). Thin patches of film form along this rim of pinched film. These thin patches move away from the border and displace the thicker film at the top of the bubble. These highly nonlinear, convective plumes drive the drainage over the bubble and enhance mixing inside the thin liquid film. In § 2.2 of Lhuissier & Villermaux (2012) the authors conducted an extensive study of film drainage over a freely suspended air bubble and found that the wavelength of the convection cells scales with bubble size and film thickness, and evolves in time (see figures 11 and 12(b) of Lhuissier & Villermaux 2012).

At first glance, the characteristic rising plumes in the marginal regeneration process is not present in our system. However, if one were to define marginal regeneration as a process that is initiated with film thickness fluctuations along the rim of the film (i.e. the location of the minimum film thickness) and thinner liquid moves from the rim into the thin film region, thereby displacing the thicker film in the film region into the bulk region, then the film evolution described in this study is a type of marginal regeneration. Gros *et al.* (2021) studied marginal regeneration in horizontal surfactant films that suppress the effects of gravity. Figure 2(d) in the Gros system depicts the evolution of the film thickness profile, where film thickness fluctuations form near the meniscus and patches of thin film grow and coalesce. Despite the lack of the characteristic rising plumes, the authors found good agreement between their system and systems where the rising plumes are present. The onset of the instability described in the Gros study is similar to the present study. Furthermore, in our system, the wavenumber associated with the most dangerous mode in the linear stability analysis is different from the wavenumber of the film ridges during the stage where the dimple rapidly discharges (figure 2(b)5 versus figure 2(b)6–9). This difference suggests the presence of nonlinear effects that drive the development of the non-axisymmetric plumes observed in our system.

## 5. Conclusion

In this paper we consider the behaviour of a soluble surfactant film over an air bubble. Through experimental observations and numerical simulations, we capture the onset of symmetry breaking associated with the emergence of an air bubble from an aqueous solution of Triton X-100 below the critical micelle concentration. As the air bubble emerges from the solution, a thin liquid film is formed atop the air bubble. After the bubble has penetrated the initially flat air–liquid interface, the bubble is held in place. Thereafter, the previously axisymmetric film succumbs to ambient disturbances and symmetry breaking ensues. In both the experiment and the parameter matched simulation, the perturbation associated with intermediate wavenumbers exhibit the fastest growth.

A linear stability analysis is conducted to elucidate the mechanism behind the disturbance growth. Similar to a previous study in surfactant spreading (Warner *et al.* 2004), we find that the disturbance acts to locally thicken the film while creating an azimuthal surfactant gradient that acts to bring more liquid into the already thickened local region, thereby contributing to the growth of the disturbance.



Finally, we examine the effect of bubble protrusion on the maximum growth rate wavenumber,  $m_{max}$ . As the bubble protrusion increases, so does the circumference of the rim,  $R$ , where the disturbances initially act upon the system. Analysis of the base state film thickness profiles and the adsorbed surfactant gradients reveals that the width over which the radial direction flow driving force has an appreciable amplitude ( $\Delta R$ ) is another important system length scale. Scaling analysis reveals that  $m_{max} \sim 2R/\Delta R$ .

In summary, this work gives a comprehensive examination of the symmetry breaking phenomenon associated with a soap bubble emerging from a soap bath. With the theoretical framework introduced in this paper, others may use the tools we have developed to examine other thin film systems that evolve on a curved substrate – a commonly encountered geometry. Future work may involve (1) examining the shear and dilatational effects of insoluble surfactants on an interface by using the Boussinesq–Scriven model, (2) increasing the numerical spatial resolution to allow for more azimuthal refinement, (3) incorporating bubble surface deformation to the model formulation, and (4) investigating the nonlinear flows that occur after the onset of instability.

**Funding.** This paper is based upon work supported by the National Science Foundation under grant no. CBET – 1952635.

**Declaration of interests.** The authors report no conflict of interest.

**Author ORCIDs.**

 Xingyi Shi <https://orcid.org/0000-0003-3547-6431>.

## Appendix A

### A.1. Derivation of the governing equations

#### A.1.1. Geometry

Let the shape functions for the top and the bottom interfaces be  $f_1 = z - h_1(t, r, \theta)$  and  $f_2 = z - h_2(t, r, \theta)$ . The surface normal vectors point from the gas phase into the liquid phase. Following these definitions, the unit normals are

$$\mathbf{n}_1 = -\frac{\nabla f_1}{\|\nabla f_1\|} = \frac{1}{S_1} \left( \sqrt{\epsilon} \frac{\partial h_1}{\partial r} \mathbf{e}_r + \sqrt{\epsilon} \frac{1}{r} \frac{\partial h_1}{\partial \theta} \mathbf{e}_\theta - \mathbf{e}_z \right), \quad (\text{A1})$$

$$\mathbf{n}_2 = +\frac{\nabla f_2}{\|\nabla f_2\|} = \frac{1}{S_2} \left( -\sqrt{\epsilon} \frac{\partial h_1}{\partial r} \mathbf{e}_r - \sqrt{\epsilon} \frac{1}{r} \frac{\partial h_1}{\partial \theta} \mathbf{e}_\theta + \mathbf{e}_z \right), \quad (\text{A2})$$

where  $S_1^2 = 1 + \epsilon(\partial h_1/\partial r)^2 + \epsilon((1/r)(\partial h_1/\partial \theta))^2$ , and  $S_2^2 = 1 + \epsilon(\partial h_2/\partial r)^2 + \epsilon((1/r)(\partial h_2/\partial \theta))^2$ . The surface tangent vectors for each interface are defined as

$$\mathbf{t}_1^1 = \sqrt{\epsilon} \frac{\partial h_1}{\partial r} \mathbf{e}_z + \mathbf{e}_r, \quad \mathbf{t}_1^2 = \sqrt{\epsilon} \frac{1}{r} \frac{\partial h_1}{\partial \theta} \mathbf{e}_z + \mathbf{e}_\theta, \quad (\text{A3a,b})$$

$$\mathbf{t}_2^1 = \sqrt{\epsilon} \frac{\partial h_2}{\partial r} \mathbf{e}_z + \mathbf{e}_r, \quad \mathbf{t}_2^2 = \sqrt{\epsilon} \frac{1}{r} \frac{\partial h_2}{\partial \theta} \mathbf{e}_z + \mathbf{e}_\theta. \quad (\text{A4a,b})$$

The mean curvatures  $\kappa_1$  and  $\kappa_2$  are defined as

$$\kappa_1 = \nabla \cdot \mathbf{n}_1 = \frac{1}{r} \frac{\partial}{\partial r} \left( r \frac{1}{S_1} \frac{\partial h_1}{\partial r} \right) + \frac{1}{r} \frac{\partial}{\partial \theta} \left( \frac{1}{S_1} \frac{1}{r} \frac{\partial h_1}{\partial \theta} \right), \quad (\text{A5})$$

$$\kappa_2 = \nabla \cdot \mathbf{n}_2 = \frac{1}{r} \frac{\partial}{\partial r} \left( r \frac{1}{S_2} \frac{\partial h_2}{\partial r} \right) + \frac{1}{r} \frac{\partial}{\partial \theta} \left( \frac{1}{S_2} \frac{1}{r} \frac{\partial h_2}{\partial \theta} \right). \quad (\text{A6})$$

For the sake of completeness, we also provide the expressions for various surface operators used in the subsequent derivation.

The surface Laplacian for a scalar function  $f$  on surface  $i$  is defined as

$$\nabla_s^2 f = \nabla^2 f - (\nabla \cdot \mathbf{n}_i)(\mathbf{n}_i \cdot \nabla f) - \mathbf{n}_i^T \cdot \nabla (\nabla f) \cdot \mathbf{n}_i. \tag{A7}$$

After some algebra, one may obtain

$$\begin{aligned} \nabla_s^2 f &= \frac{1}{\epsilon^2} \frac{\partial^2 f}{\partial z^2} + \frac{1}{\epsilon} \frac{1}{r} \frac{\partial}{\partial r} \left( r \frac{\partial f}{\partial r} \right) + \frac{1}{\epsilon} \frac{1}{r^2} \frac{\partial^2 f}{\partial \theta^2} \\ &\quad - \frac{\kappa_i}{S_i} \left( -\frac{1}{\epsilon} \frac{\partial f}{\partial z} + \frac{\partial f}{\partial r} \frac{\partial h_i}{\partial r} + \frac{1}{r} \frac{\partial f}{\partial \theta} \frac{1}{r} \frac{\partial h_i}{\partial \theta} \right) \\ &\quad + \frac{1}{S_i^2} \left( -\frac{1}{\epsilon^2} \frac{\partial^2 f}{\partial z^2} + \frac{1}{\epsilon} \frac{\partial}{\partial r} \left( \frac{\partial f}{\partial z} \right) \frac{\partial h_i}{\partial r} + \frac{1}{\epsilon} \frac{1}{r} \frac{\partial}{\partial \theta} \left( \frac{\partial f}{\partial z} \right) \frac{1}{r} \frac{\partial h_i}{\partial \theta} \right) \\ &\quad + \frac{1}{S_i^2} \left( \frac{1}{\epsilon} \frac{\partial}{\partial z} \left( \frac{\partial f}{\partial r} \right) \frac{\partial h_i}{\partial r} - \frac{\partial^2 f}{\partial r^2} \left( \frac{\partial h_i}{\partial r} \right)^2 - \frac{1}{r} \frac{\partial}{\partial \theta} \left( \frac{\partial f}{\partial r} \right) \frac{1}{r} \frac{\partial h_i}{\partial \theta} \frac{\partial h_i}{\partial r} \right) \\ &\quad + \frac{1}{S_i^2} \left( \frac{1}{\epsilon} \frac{\partial}{\partial z} \left( \frac{1}{r} \frac{\partial f}{\partial \theta} \right) \frac{1}{r} \frac{\partial h_i}{\partial \theta} - \frac{\partial}{\partial r} \left( \frac{1}{r} \frac{\partial f}{\partial \theta} \right) \frac{\partial h_i}{\partial r} \frac{1}{r} \frac{\partial h_i}{\partial \theta} - \frac{1}{r^2} \frac{\partial^2 f}{\partial \theta^2} \left( \frac{1}{r} \frac{\partial h_i}{\partial \theta} \right)^2 \right). \end{aligned} \tag{A8}$$

The surface gradient operator is defined as

$$\nabla_{s,i} = (\mathbf{I} - \mathbf{n}_i \mathbf{n}_i) \cdot \nabla \tag{A9}$$

$$\begin{aligned} &= \mathbf{e}_z \frac{1}{S_i^2} \left( \left( \left( \frac{\partial h_i}{\partial r} \right)^2 + \left( \frac{1}{r} \frac{\partial h_i}{\partial \theta} \right)^2 \right) \frac{\partial}{\partial z} + \frac{\partial h_i}{\partial r} \frac{\partial}{\partial r} + \frac{1}{r} \frac{\partial h_i}{\partial \theta} \frac{1}{r} \frac{\partial}{\partial \theta} \right) \\ &\quad + \mathbf{e}_r \frac{1}{S_i^2} \frac{1}{\epsilon^{1/2}} \left( \frac{\partial h_i}{\partial r} \frac{\partial}{\partial z} + \left( 1 + \epsilon \left( \frac{1}{r} \frac{\partial h_i}{\partial \theta} \right)^2 \right) \frac{\partial}{\partial r} - \epsilon \frac{\partial h_i}{\partial r} \frac{1}{r} \frac{\partial h_i}{\partial \theta} \frac{1}{r} \frac{\partial}{\partial \theta} \right) \\ &\quad + \mathbf{e}_\theta \frac{1}{S_i^2} \frac{1}{\epsilon^{1/2}} \left( \frac{1}{r} \frac{\partial h_i}{\partial \theta} \frac{\partial}{\partial z} - \epsilon \frac{\partial h_i}{\partial r} \frac{1}{r} \frac{\partial h_i}{\partial \theta} \frac{\partial}{\partial r} + \left( 1 + \epsilon \left( \frac{\partial h_i}{\partial r} \right)^2 \right) \frac{1}{r} \frac{\partial}{\partial \theta} \right). \end{aligned} \tag{A10}$$

Here we provide the detailed expression for the surface divergence operator for surface  $i$  applied to a vector,  $\mathbf{F}$ ,

$$\begin{aligned} \nabla_s \cdot \mathbf{F} &= \frac{1}{S_i^2} \left( \left( \left( \frac{\partial h_i}{\partial r} \right)^2 + \left( \frac{1}{r} \frac{\partial h_i}{\partial \theta} \right)^2 \right) \frac{\partial F_z}{\partial z} + \frac{1}{\epsilon^{1/2}} \frac{\partial h_i}{\partial r} \frac{\partial F_r}{\partial z} + \frac{1}{\epsilon^{1/2}} \frac{1}{r} \frac{\partial h_i}{\partial \theta} \frac{\partial F_\theta}{\partial z} \right) \\ &\quad + \frac{1}{S_i^2} \left( \frac{\partial h_i}{\partial r} \frac{1}{r} \frac{\partial}{\partial r} (r F_z) + \frac{1}{\epsilon^{1/2}} \left( 1 + \epsilon \left( \frac{1}{r} \frac{\partial h_i}{\partial \theta} \right)^2 \right) \frac{1}{r} \frac{\partial}{\partial r} (r F_r) \right) \end{aligned}$$

$$\begin{aligned}
 & -\epsilon^{1/2} \frac{1}{r} \frac{\partial h_i}{\partial \theta} \frac{\partial h_i}{\partial r} \frac{1}{r} \frac{\partial}{\partial r} (r F_\theta) \\
 & + \frac{1}{S_i^2} \left( \frac{1}{r} \frac{\partial h_i}{\partial \theta} \frac{1}{r} \frac{\partial F_z}{\partial \theta} - \epsilon^{1/2} \frac{1}{r} \frac{\partial h_i}{\partial \theta} \frac{\partial h_i}{\partial r} \frac{1}{r} \frac{\partial F_r}{\partial \theta} + \frac{1}{\epsilon^{1/2}} \left( 1 + \epsilon \left( \frac{\partial h_i}{\partial r} \right)^2 \right) \frac{1}{r} \frac{\partial F_\theta}{\partial \theta} \right).
 \end{aligned} \tag{A11}$$

In-plane surface velocity at the two interfaces can be expressed as  $\mathbf{u}_{s,i}^* = (\mathbf{I} - \mathbf{n}_i \mathbf{n}_i) \cdot \mathbf{u}^*|_{h_i}$ , where  $\mathbf{u}^*|_{h_i} = u_z \mathbf{e}_z + (1/\epsilon^{1/2}) u_r \mathbf{e}_r + (1/\epsilon^{1/2}) u_\theta \mathbf{e}_\theta$ . The subscript  $i = 1, 2$  represents the top and bottom interfaces. After some algebraic manipulations, one can get the following detailed expression:

$$\begin{aligned}
 \mathbf{u}_{s,i} &= \frac{\mathbf{e}_z}{S_i^2} \left( \epsilon \left( \left( \frac{\partial h_i}{\partial r} \right)^2 + \left( \frac{1}{r} \frac{\partial h_i}{\partial \theta} \right)^2 \right) u_z + \frac{\partial h_i}{\partial r} u_r + \frac{1}{r} \frac{\partial h_i}{\partial \theta} u_\theta \right) \\
 &+ \frac{\mathbf{e}_r}{S_i^2} \left( \epsilon^{1/2} \frac{\partial h_i}{\partial r} u_z + \frac{1}{\epsilon^{1/2}} \left( 1 + \epsilon \left( \frac{1}{r} \frac{\partial h_i}{\partial \theta} \right)^2 \right) u_r - \epsilon^{1/2} \frac{1}{r} \frac{\partial h_i}{\partial \theta} \frac{\partial h_i}{\partial r} u_\theta \right) \\
 &+ \frac{\mathbf{e}_\theta}{S_i^2} \left( \epsilon^{1/2} \frac{1}{r} \frac{\partial h_i}{\partial \theta} u_z - \epsilon^{1/2} \frac{1}{r} \frac{\partial h_i}{\partial \theta} \frac{\partial h_i}{\partial r} u_r + \frac{1}{\epsilon^{1/2}} \left( 1 + \epsilon \left( \frac{\partial h_i}{\partial r} \right)^2 \right) u_\theta \right).
 \end{aligned} \tag{A12}$$

### A.1.2. Mass and momentum balances

The non-dimensionalized continuity equation for a Newtonian, incompressible liquid is

$$\frac{\partial v_z}{\partial z} + \frac{1}{r} \frac{\partial}{\partial r} (r v_r) + \frac{1}{r} \frac{\partial v_\theta}{\partial \theta} = 0, \tag{A13}$$

and the associated kinematic boundary condition at the two liquid–air interfaces is

$$\frac{\partial h_i}{\partial t} - v_z|_{h_i} + v_r|_{h_i} \frac{\partial h_i}{\partial r} + v_\theta|_{h_i} \frac{1}{r} \frac{\partial h_i}{\partial \theta} = 0, \tag{A14}$$

where the subscript  $i = 1, 2$  represents the top and bottom interfaces. We integrate the continuity equation with respect to  $z$  and apply the kinematic boundary conditions to get the following mass balance inside the liquid film:

$$\frac{\partial h}{\partial t} + \frac{1}{r} \frac{\partial}{\partial r} (r h \langle v_r \rangle) + \frac{1}{r} \frac{\partial}{\partial \theta} (h \langle v_\theta \rangle) = 0. \tag{A15}$$

Here  $h \equiv h_1 - h_2$ ,  $\int_{h_2}^{h_1} v_r dz = h \langle v_r \rangle$  and  $\int_{h_2}^{h_1} v_\theta dz = h \langle v_\theta \rangle$ .

Neglect all inertial effects and the resulting Stokes equations are

$$\frac{\partial P}{\partial z} = -\frac{Bo}{Ca} + \epsilon \frac{\partial^2 v_z}{\partial z^2} + \epsilon^2 \left( \frac{1}{r} \frac{\partial}{\partial r} \left( r \frac{\partial v_z}{\partial r} \right) + \frac{1}{r^2} \frac{\partial^2 v_z}{\partial \theta^2} \right), \tag{A16}$$

$$\frac{\partial P}{\partial r} = \frac{\partial^2 v_r}{\partial z^2} + \epsilon \left( \frac{\partial}{\partial r} \left( \frac{1}{r} \frac{\partial}{\partial r} (r v_r) \right) + \frac{1}{r^2} \frac{\partial^2 v_r}{\partial \theta^2} - \frac{2}{r^2} \frac{\partial v_\theta}{\partial \theta} \right) \tag{A17}$$

and

$$\frac{1}{r} \frac{\partial P}{\partial \theta} = \frac{\partial^2 v_\theta}{\partial z^2} + \epsilon \left( \frac{\partial}{\partial r} \left( \frac{1}{r} \frac{\partial}{\partial r} (r v_\theta) \right) + \frac{1}{r^2} \frac{\partial^2 v_\theta}{\partial \theta^2} + \frac{2}{r^2} \frac{\partial v_r}{\partial \theta} \right). \tag{A18}$$

A.1.3. Surfactant mass transport

The motion of the lower interface approaching the top interface drives liquid flow inside the thin film. As a result, the surfactant distributions at the interfaces are driven away from equilibrium. Because the local surfactant concentration is related to the surface tension, it is necessary to examine the relationship between the liquid flow inside the thin film and the distribution of the surfactants at the interfaces. In the bulk the surfactant concentration is governed by the following advection–diffusion equation:

$$\frac{\partial c}{\partial t} + \frac{\partial c}{\partial z} v_z + \frac{\partial c}{\partial r} v_r + \frac{1}{r} \frac{\partial c}{\partial \theta} v_\theta = \frac{1}{Pe} \left( \frac{1}{\epsilon} \frac{\partial^2 c}{\partial z^2} + \frac{1}{r} \frac{\partial}{\partial r} \left( r \frac{\partial c}{\partial r} \right) + \frac{1}{r^2} \frac{\partial^2 c}{\partial \theta^2} \right). \tag{A19}$$

Surfactants can adsorb and desorb at both the top and bottom air–liquid interfaces,

$$j_{n1}^* = (j_{ads}^* - j_{des}^*)|_{h_1^*} = \mathbf{n}_{\text{bulk to h1}} \cdot \mathbf{J}^* = -\mathbf{n}_1 \cdot (-D\nabla^* c^*)|_{h_1^*}, \tag{A20}$$

$$j_{n2}^* = (j_{ads}^* - j_{des}^*)|_{h_2^*} = \mathbf{n}_{\text{bulk to h2}} \cdot \mathbf{J}^* = -\mathbf{n}_2 \cdot (-D\nabla^* c^*)|_{h_2^*}, \tag{A21}$$

where  $j_{des}^*$  and  $j_{ads}^*$  are desorption and adsorption fluxes at the interface. Non-dimensionalize to get

$$\frac{1}{S_1} \left( -\frac{1}{\epsilon} \frac{\partial c}{\partial z} + \frac{\partial c}{\partial r} \frac{\partial h_1}{\partial r} + \frac{1}{r} \frac{\partial c}{\partial \theta} \frac{1}{r} \frac{\partial h_1}{\partial \theta} \right) \Big|_{h_1} = Pe\beta j_{n1}, \tag{A22}$$

$$\frac{1}{S_2} \left( -\frac{1}{\epsilon} \frac{\partial c}{\partial z} + \frac{\partial c}{\partial r} \frac{\partial h_2}{\partial r} + \frac{1}{r} \frac{\partial c}{\partial \theta} \frac{1}{r} \frac{\partial h_2}{\partial \theta} \right) \Big|_{h_2} = -Pe\beta j_{n2}. \tag{A23}$$

It is interesting to note that at  $O(1)$  the governing equation and the boundary conditions for  $c^{(0)}$  are

$$\frac{\partial^2 c^{(0)}}{\partial z^2} = 0 \quad \text{and} \quad \frac{\partial c^{(0)}}{\partial z} \Big|_{h_1^{(0)}, h_2^{(0)}} = 0, \tag{A24a,b}$$

and it follows that

$$c^{(0)} = c^{(0)}(t, r, \theta). \tag{A25}$$

The transport of adsorbed surfactants is defined by

$$\frac{\partial \Gamma_i^*}{\partial t^*} + \nabla_s^* \cdot (\Gamma_i^* \mathbf{u}_{s,i}^*) + \Gamma_i^* (\nabla_s^* \cdot \mathbf{n}_i) (\mathbf{u}^* \cdot \mathbf{n}_i) - D_s \nabla_s^{*2} \Gamma_i^* = j_{ni}^*. \tag{A26}$$

Non-dimensionalize the above equation to get

$$\frac{\partial \Gamma_1}{\partial t} + \epsilon \nabla_s \cdot (\Gamma_1 \mathbf{u}_{s,1}) + \epsilon \Gamma_1 \kappa_1 \left( -u_z + u_r \frac{\partial h_1}{\partial r} + u_\theta \frac{1}{r} \frac{\partial h_1}{\partial \theta} \right) \Big|_{h_1} - \frac{\epsilon}{Pe_S} \nabla_{s,1}^2 \Gamma_1 = j_{n1} \tag{A27}$$

and

$$\frac{\partial \Gamma_2}{\partial t} + \epsilon \nabla_s \cdot (\Gamma_2 \mathbf{u}_{s,2}) + \epsilon \Gamma_2 \kappa_2 \left( u_z - u_r \frac{\partial h_2}{\partial r} - u_\theta \frac{1}{r} \frac{\partial h_2}{\partial \theta} \right) \Big|_{h_2} - \frac{\epsilon}{Pe_S} \nabla_{s,2}^2 \Gamma_2 = j_{n2}. \tag{A28}$$

Expressions for the surface gradient operator ( $\nabla_{s,i}^*$ ), the surface Laplacian operator ( $\nabla_{s,i}^{*2}$ ), the mean curvatures ( $\kappa_i$ ) and the surface velocities ( $\mathbf{u}_{s,i}$ ) can be found in the geometry section. For a surfactant that follows the Langmuir isotherm,  $j_{ni} = \alpha (c(\Gamma_i - 1) - \Gamma/La)$ .

**A.1.4. Stress balance**

Stress balances account for the jump in the stress across the interfaces. We can neglect the contribution of the gas phases because they are generally 1000 times less viscous than the liquid phase. In other words, the following simplifications can be applied:

$$\mathbf{n}_i \cdot (\boldsymbol{\sigma} - \boldsymbol{\sigma}_i) \cdot \mathbf{n}_i = \frac{\gamma_i}{Ca} (\nabla \cdot \mathbf{n}_i) \Rightarrow \mathbf{n}_i \cdot \boldsymbol{\sigma} \cdot \mathbf{n}_i = \frac{\gamma_i}{Ca} (\nabla \cdot \mathbf{n}_i); \tag{A29}$$

$$\mathbf{t}_i^j \cdot (\boldsymbol{\sigma} - \boldsymbol{\sigma}_i) \cdot \mathbf{n}_i = -\frac{1}{\epsilon Ca} \mathbf{t}_i^j \cdot \nabla \gamma_i \Rightarrow \mathbf{t}_i^j \cdot \boldsymbol{\sigma} \cdot \mathbf{n}_i = -\frac{1}{Ca} \mathbf{t}_i^j \cdot \nabla_s \gamma_i. \tag{A30}$$

Here  $\gamma_i$  is the local surface tension on interface  $i$ ,  $\boldsymbol{\sigma} = -P\boldsymbol{\delta} + \boldsymbol{\tau}$  is the total stress,  $i = 1, 2$  represents the interfaces and  $j = 1, 2$  represents the surface tangent directions. In this model we neglect the deformation of the lower surface. As a result, only the normal stress balance on the top interface will be considered from this point onward.

For an incompressible Newtonian fluid, the components of the viscous stress tensor,  $\boldsymbol{\tau}$ , in the cylindrical coordinate in our chosen scale are

$$\tau_{zz} = 2\epsilon \frac{\partial v_z}{\partial z}, \tag{A31}$$

$$\tau_{rr} = 2\epsilon \frac{\partial v_r}{\partial r}, \tag{A32}$$

$$\tau_{\theta\theta} = 2\epsilon \left( \frac{v_r}{r} + \frac{1}{r} \frac{\partial v_\theta}{\partial \theta} \right), \tag{A33}$$

$$\tau_{zr} = \tau_{rz} = \epsilon^{1/2} \left( \frac{\partial v_r}{\partial z} + \epsilon \frac{\partial v_z}{\partial r} \right), \tag{A34}$$

$$\tau_{z\theta} = \tau_{\theta z} = \epsilon^{1/2} \left( \frac{\partial v_\theta}{\partial z} + \epsilon \frac{1}{r} \frac{\partial v_z}{\partial \theta} \right), \tag{A35}$$

$$\tau_{r\theta} = \tau_{\theta r} = \epsilon \left( \frac{1}{r} \frac{\partial v_r}{\partial \theta} + r \frac{\partial}{\partial r} \left( \frac{v_\theta}{r} \right) \right). \tag{A36}$$

**A.1.5. The  $O(1)$  rearranged equations**

Expand all variables,  $\psi = \psi^{(0)} + \epsilon \psi^{(1)} + \epsilon^2 \psi^{(2)} + \dots$ , and extract the  $O(1)$  equation from the governing equations. Here we document the results from rearranging the  $O(1)$  equations. The mass and species balances are

$$\frac{\partial h^{(0)}}{\partial t} + \frac{1}{r} \frac{\partial}{\partial r} (r h^{(0)} \langle v_r \rangle^{(0)}) + \frac{1}{r} \frac{\partial}{\partial \theta} (h^{(0)} \langle v_\theta \rangle^{(0)}) = 0, \tag{A37}$$

$$\begin{aligned} & \frac{\partial c^{(0)}}{\partial t} + \langle v_r \rangle^{(0)} \frac{\partial c^{(0)}}{\partial r} + \langle v_\theta \rangle^{(0)} \frac{1}{r} \frac{\partial c^{(0)}}{\partial \theta} - \frac{1}{Pe} \left( \frac{1}{r} \frac{\partial}{\partial r} \left( r \frac{\partial c^{(0)}}{\partial r} \right) + \frac{1}{r^2} \frac{\partial^2 c^{(0)}}{\partial \theta^2} \right) \\ & - \frac{1}{Pe} \frac{1}{h^{(0)}} \left( \frac{\partial h^{(0)}}{\partial r} \frac{\partial c^{(0)}}{\partial r} + \frac{1}{r} \frac{\partial h^{(0)}}{\partial \theta} \frac{1}{r} \frac{\partial c^{(0)}}{\partial \theta} \right) = -\frac{\beta}{h^{(0)}} (j_{n1} + j_{n2}), \end{aligned} \tag{A38}$$

$$\begin{aligned} \frac{\partial \Gamma_1^{(0)}}{\partial t} + \frac{1}{r} \frac{\partial}{\partial r} (r \Gamma_1^{(0)} v_r^{(0)}|_{h_1^{(0)}}) + \frac{1}{r} \frac{\partial}{\partial \theta} (\Gamma_1^{(0)} v_\theta^{(0)}|_{h_1^{(0)}}) \\ - \frac{1}{Pe_S} \left( \frac{1}{r} \frac{\partial}{\partial r} \left( r \frac{\partial \Gamma_1^{(0)}}{\partial r} \right) + \frac{1}{r^2} \frac{\partial^2 \Gamma_1^{(0)}}{\partial \theta^2} \right) = j_{n1}, \end{aligned} \tag{A39}$$

$$\begin{aligned} \frac{\partial \Gamma_2^{(0)}}{\partial t} + \frac{1}{r} \frac{\partial}{\partial r} (r \Gamma_2^{(0)} v_r^{(0)}|_{h_2^{(0)}}) + \frac{1}{r} \frac{\partial}{\partial \theta} (\Gamma_2^{(0)} v_\theta^{(0)}|_{h_2^{(0)}}) \\ - \frac{1}{Pe_S} \left( \frac{1}{r} \frac{\partial}{\partial r} \left( r \frac{\partial \Gamma_2^{(0)}}{\partial r} \right) + \frac{1}{r^2} \frac{\partial^2 \Gamma_2^{(0)}}{\partial \theta^2} \right) = j_{n2}. \end{aligned} \tag{A40}$$

Integrate the momentum balance in the  $z$  direction with respect to  $z$  to get

$$\frac{\partial P^{(0)}}{\partial z} = -\frac{Bo}{Ca} \Rightarrow P^{(0)} = -\frac{Bo}{Ca} z + \mathcal{P}^{(0)}(t, r, \theta). \tag{A41}$$

Insert the above equation to the normal stress balance at  $O(1)$  to get

$$\frac{1}{r} \frac{\partial}{\partial r} \left( r \frac{\partial h_1^{(0)}}{\partial r} \right) + \frac{1}{r^2} \frac{\partial^2 h_1^{(0)}}{\partial \theta^2} = -Ca \mathcal{P}^{(0)} + Boh_1^{(0)}. \tag{A42}$$

The momentum balances at  $O(1)$  in  $r$  and  $\theta$  are

$$\frac{\partial v_r^{(0)}}{\partial z} \Big|_{h_2^{(0)}}^{h_1^{(0)}} = h^{(0)} \frac{\partial \mathcal{P}^{(0)}}{\partial r}, \tag{A43}$$

$$\frac{\partial v_\theta^{(0)}}{\partial z} \Big|_{h_2^{(0)}}^{h_1^{(0)}} = h^{(0)} \frac{1}{r} \frac{\partial \mathcal{P}^{(0)}}{\partial \theta}, \tag{A44}$$

and the tangential stress balances are

$$-\frac{\partial v_r^{(0)}}{\partial z} \Big|_{h_1^{(0)}} = -\frac{1}{\epsilon Ca} \frac{\partial -\Pi_1^{(0)}}{\partial r}, \quad + \frac{\partial v_r^{(0)}}{\partial z} \Big|_{h_2^{(0)}} = -\frac{1}{\epsilon Ca} \frac{\partial -\Pi_2^{(0)}}{\partial r}, \tag{A45a,b}$$

$$-\frac{\partial v_\theta^{(0)}}{\partial z} \Big|_{h_1^{(0)}} = -\frac{1}{\epsilon Ca} \frac{1}{r} \frac{\partial -\Pi_1^{(0)}}{\partial \theta}, \quad + \frac{\partial v_\theta^{(0)}}{\partial z} \Big|_{h_2^{(0)}} = -\frac{1}{\epsilon Ca} \frac{1}{r} \frac{\partial -\Pi_2^{(0)}}{\partial \theta}. \tag{A46a,b}$$

Combining the above we obtain

$$h^{(0)} \frac{\partial \mathcal{P}^{(0)}}{\partial r} = \frac{1}{\epsilon Ca} \left( \frac{\partial -\Pi_1^{(0)}}{\partial r} + \frac{\partial -\Pi_2^{(0)}}{\partial r} \right), \tag{A47}$$

$$h^{(0)} \frac{1}{r} \frac{\partial \mathcal{P}^{(0)}}{\partial \theta} = \frac{1}{\epsilon Ca} \left( \frac{1}{r} \frac{\partial -\Pi_1^{(0)}}{\partial \theta} + \frac{1}{r} \frac{\partial -\Pi_2^{(0)}}{\partial \theta} \right). \tag{A48}$$

Note that we need to know the surface velocities for the transport equations for the adsorbed surfactants. Here we shall derive some expressions that relate  $v_r^{(0)}|_{h_i}$  and  $v_\theta^{(0)}|_{h_i}$



to pressure, depth-averaged velocities and surface tension gradients. Let us focus on the radial direction equations (for the azimuthal direction, just change the subscripts and the derivatives). At  $O(1)$  the radial direction momentum balance is

$$\frac{\partial^2 v_r^{(0)}}{\partial z^2} = \frac{\partial \mathcal{P}^{(0)}}{\partial r}. \quad (\text{A49})$$

Let  $v_r^{(0)}|_{h_1} \equiv v_{r,s1}$ ,  $v_r^{(0)}|_{h_2} \equiv v_{r,s2}$ , and integrate the above equation twice with respect to  $z$ , to get

$$v_r^{(0)} = \frac{1}{2} \frac{\partial \mathcal{P}^{(0)}}{\partial r} (z - h_1^{(0)})(z - h_2^{(0)}) + v_{r,s1} \frac{z - h_2^{(0)}}{h^{(0)}} + v_{r,s2} \frac{h_1^{(0)} - z}{h^{(0)}}. \quad (\text{A50})$$

Integrating once more we obtain

$$\langle v_r \rangle^{(0)} = -\frac{(h^{(0)})^2}{12} \frac{\partial \mathcal{P}^{(0)}}{\partial r} + \frac{1}{2}(v_{r,s1} + v_{r,s2}). \quad (\text{A51})$$

Now we can relate the surface velocities to the pressure gradient via the tangential stress balances in the radial direction, i.e.

$$\left. \frac{\partial v_r^{(0)}}{\partial z} \right|_{h_1^{(0)}} = +\frac{h^{(0)}}{2} \frac{\partial \mathcal{P}^{(0)}}{\partial r} + (v_{r,s1} - v_{r,s2})/h^{(0)} = +\frac{1}{\epsilon Ca} \frac{\partial - \Pi_1^{(0)}}{\partial r}, \quad (\text{A52})$$

$$\left. \frac{\partial v_r^{(0)}}{\partial z} \right|_{h_2^{(0)}} = -\frac{h^{(0)}}{2} \frac{\partial \mathcal{P}^{(0)}}{\partial r} + (v_{r,s1} - v_{r,s2})/h^{(0)} = -\frac{1}{\epsilon Ca} \frac{\partial - \Pi_2^{(0)}}{\partial r}, \quad (\text{A53})$$

$$v_{r,s1} - v_{r,s2} = \frac{1}{2} \frac{h^{(0)}}{\epsilon Ca} \left( \frac{\partial - \Pi_1^{(0)}}{\partial r} - \frac{\partial - \Pi_2^{(0)}}{\partial r} \right). \quad (\text{A54})$$

Using (A51) and (A54), we obtain

$$v_r^{(0)}|_{h_1} = v_{r,s1} = \langle v_r \rangle^{(0)} + \frac{(h^{(0)})^2}{12} \frac{\partial \mathcal{P}^{(0)}}{\partial r} + \frac{1}{4} \frac{h^{(0)}}{\epsilon Ca} \left( \frac{\partial - \Pi_1^{(0)}}{\partial r} - \frac{\partial - \Pi_2^{(0)}}{\partial r} \right), \quad (\text{A55})$$

$$v_r^{(0)}|_{h_2} = v_{r,s2} = \langle v_r \rangle^{(0)} + \frac{(h^{(0)})^2}{12} \frac{\partial \mathcal{P}^{(0)}}{\partial r} - \frac{1}{4} \frac{h^{(0)}}{\epsilon Ca} \left( \frac{\partial - \Pi_1^{(0)}}{\partial r} - \frac{\partial - \Pi_2^{(0)}}{\partial r} \right). \quad (\text{A56})$$

Similarly, in the azimuthal direction,

$$v_\theta^{(0)}|_{h_1} = \langle v_\theta \rangle^{(0)} + \frac{(h^{(0)})^2}{12} \frac{1}{r} \frac{\partial \mathcal{P}^{(0)}}{\partial \theta} + \frac{1}{4} \frac{h^{(0)}}{\epsilon Ca} \left( \frac{1}{r} \frac{\partial - \Pi_1^{(0)}}{\partial \theta} - \frac{1}{r} \frac{\partial - \Pi_2^{(0)}}{\partial \theta} \right), \quad (\text{A57})$$

$$v_\theta^{(0)}|_{h_2} = \langle v_\theta \rangle^{(0)} + \frac{(h^{(0)})^2}{12} \frac{1}{r} \frac{\partial \mathcal{P}^{(0)}}{\partial \theta} - \frac{1}{4} \frac{h^{(0)}}{\epsilon Ca} \left( \frac{1}{r} \frac{\partial - \Pi_1^{(0)}}{\partial \theta} - \frac{1}{r} \frac{\partial - \Pi_2^{(0)}}{\partial \theta} \right). \quad (\text{A58})$$

Before proceeding with the rest of the derivation, some observations and simplifications should be made regarding the symmetry in governing equations for the adsorbed surfactant species. In this study it is assumed that surface curvature has no effect on the equilibrium

distribution of the surfactant on the interfaces. As such,  $\Gamma_1(t = 0) = \Gamma_2(t = 0) = \Gamma_0/\Gamma_\infty$ . In the azimuthal direction both variables are subjected to the same boundary condition:  $\Gamma_i(\theta) = \Gamma_i(\theta + 2\pi)$ . In the radial direction, on both interfaces, it is assumed that as  $r \rightarrow \infty$ , the surface adsorbed species approaches the same equilibrium value of  $\Gamma_0/\Gamma_\infty$ . If one were to solve for  $\Gamma_1^{(0)}$  and  $\Gamma_2^{(0)}$ , with the above initial and boundary conditions, the partial differential equations will solve to  $\Gamma_1^{(0)} = \Gamma_2^{(0)}$ . This solution should not be surprising, because with  $\Gamma_1^{(0)} = \Gamma_2^{(0)}$ , then  $\Pi_1^{(0)} = \Pi_2^{(0)}$  and the surface velocities at the interfaces are the same for both the radial and the azimuthal directions:  $v_r^{(0)}|_{h_1} = v_r^{(0)}|_{h_2}$  and  $v_\theta^{(0)}|_{h_1} = v_\theta^{(0)}|_{h_2}$ . As a result, (A39) and (A40) are the same, except for the subscript. Furthermore, because these two equations have the same initial and boundary conditions, their solutions are identical. To save on computation time, we elect to combine the two variables into a single variable governed by a single equation:  $\Gamma_1^{(0)} = \Gamma_2^{(0)} = \Gamma$ . For the rest of the derivation, this simplification will be used.

### A.1.6. The $O(\epsilon)$ equations

Note that in the absence of the surfactants (i.e.  $c^{(0)} = 0$  and  $\Gamma_i^{(0)} = 0$ ) the pressure gradient in the radial and azimuthal directions goes to zero, instead of the expected expressions for a flow created by squeezing a clean bubble. Thus, we need to examine the  $O(\epsilon)$  equations to regularize the  $O(1)$  equations. We neglect the effect of  $O(1)$  Marangoni flows on the  $O(\epsilon)$  flow. Specifically, we apply the following simplifications:

$$v_r^{(0)} \approx \langle v_r \rangle^{(0)}, \quad v_\theta^{(0)} \approx \langle v_\theta \rangle^{(0)}, \quad \frac{\partial v_z^{(0)}}{\partial z} \approx -\frac{1}{r} \frac{\partial}{\partial r} \left( r \langle v_r \rangle^{(0)} \right) - \frac{1}{r} \frac{\partial \langle v_\theta \rangle^{(0)}}{\partial \theta}. \quad (\text{A59a-c})$$

We further neglect the effects of the  $O(\epsilon)$  Marangoni flows:  $\phi^{(1)} \approx 0$ ,  $\Theta^{(1)} \approx 0$ . The mass balance at  $O(\epsilon)$  is

$$\begin{aligned} \frac{\partial h^{(1)}}{\partial t} + \frac{1}{r} \frac{\partial}{\partial r} \left( r h^{(1)} \langle v_r \rangle^{(0)} \right) + \frac{1}{r} \frac{\partial}{\partial r} \left( r h^{(0)} \langle v_r \rangle^{(1)} \right) + \frac{1}{r} \frac{\partial}{\partial \theta} \left( h^{(1)} \langle v_\theta \rangle^{(0)} \right) \\ + \frac{1}{r} \frac{\partial}{\partial \theta} \left( h^{(0)} \langle v_\theta \rangle^{(1)} \right) = 0. \end{aligned} \quad (\text{A60})$$

The  $O(\epsilon)$  normal stress balance on the top interface goes to

$$\begin{aligned} \frac{1}{r} \frac{\partial}{\partial r} \left( r \frac{\partial h_1^{(1)}}{\partial r} \right) + \frac{1}{r^2} \frac{\partial^2 h_1^{(1)}}{\partial \theta^2} = -CaP^{(1)} \Big|_{h_1^{(0)}} + Boh_1^{(1)} \\ - 2Ca \left( \frac{1}{r} \frac{\partial}{\partial r} \left( r \langle v_r \rangle^{(0)} \right) + \frac{1}{r} \frac{\partial \langle v_\theta \rangle^{(0)}}{\partial \theta} \right). \end{aligned} \quad (\text{A61})$$

The  $O(\epsilon)$  momentum balances are

$$\frac{\partial P^{(1)}}{\partial z} = \frac{\partial^2 v_z^{(0)}}{\partial z^2} \Rightarrow P^{(1)} = \frac{\partial v_z^{(0)}}{\partial z} + \mathcal{P}^{(1)}(t, r, \theta) \approx P^{(1)}(t, r, \theta); \quad (\text{A62})$$

*Instability of surfactant films*

$$\frac{\partial P^{(1)}}{\partial r} = \frac{\partial^2 v_r^{(1)}}{\partial z^2} + \frac{\partial}{\partial r} \left( \frac{1}{r} \frac{\partial}{\partial r} \left( r \langle v_r \rangle^{(0)} \right) \right) + \frac{1}{r^2} \frac{\partial^2 \langle v_r \rangle^{(0)}}{\partial \theta^2} - \frac{2}{r^2} \frac{\partial \langle v_\theta \rangle^{(0)}}{\partial \theta}, \quad (\text{A63})$$

$$\frac{1}{r} \frac{\partial P^{(1)}}{\partial \theta} = \frac{\partial^2 v_\theta^{(1)}}{\partial z^2} + \frac{\partial}{\partial r} \left( \frac{1}{r} \frac{\partial}{\partial r} \left( r \langle v_\theta \rangle^{(0)} \right) \right) + \frac{1}{r^2} \frac{\partial^2 \langle v_\theta \rangle^{(0)}}{\partial \theta^2} + \frac{2}{r^2} \frac{\partial \langle v_r \rangle^{(0)}}{\partial \theta}. \quad (\text{A64})$$

The  $O(\epsilon)$  tangential stress balances are

$$\begin{aligned} \left. \frac{\partial v_r^{(1)}}{\partial z} \right|_{h_1^{(0)}} &= 2 \frac{\partial h_1^{(0)}}{\partial r} \left( \frac{1}{r} \frac{\partial}{\partial r} \left( r \langle v_r \rangle^{(0)} \right) + \frac{1}{r} \frac{\partial \langle v_\theta \rangle^{(0)}}{\partial \theta} \right) \\ &+ h_1^{(0)} \frac{\partial}{\partial r} \left( \frac{1}{r} \frac{\partial}{\partial r} \left( r \langle v_r \rangle^{(0)} \right) + \frac{1}{r} \frac{\partial \langle v_\theta \rangle^{(0)}}{\partial \theta} \right) \\ &+ 2 \frac{\partial h_1^{(0)}}{\partial r} \frac{\partial \langle v_r \rangle^{(0)}}{\partial r} + \frac{1}{r} \frac{\partial h_1^{(0)}}{\partial \theta} \left( \frac{1}{r} \frac{\partial \langle v_r \rangle^{(0)}}{\partial \theta} + r \frac{\partial}{\partial r} \left( \frac{\langle v_\theta \rangle^{(0)}}{r} \right) \right), \end{aligned} \quad (\text{A65})$$

$$\begin{aligned} \left. \frac{\partial v_\theta^{(1)}}{\partial z} \right|_{h_1^{(0)}} &= 2 \frac{1}{r} \frac{\partial h_1^{(0)}}{\partial \theta} \left( \frac{1}{r} \frac{\partial}{\partial r} \left( r \langle v_r \rangle^{(0)} \right) + \frac{1}{r} \frac{\partial \langle v_\theta \rangle^{(0)}}{\partial \theta} \right) \\ &+ h_1^{(0)} \frac{1}{r} \frac{\partial}{\partial \theta} \left( \frac{1}{r} \frac{\partial}{\partial r} \left( r \langle v_r \rangle^{(0)} \right) + \frac{1}{r} \frac{\partial \langle v_\theta \rangle^{(0)}}{\partial \theta} \right) \\ &+ 2 \frac{1}{r} \frac{\partial h_1^{(0)}}{\partial \theta} \left( \frac{\langle v_r \rangle^{(0)}}{r} + \frac{1}{r} \frac{\partial \langle v_\theta \rangle^{(0)}}{\partial \theta} \right) \\ &+ \frac{\partial h_1^{(0)}}{\partial r} \left( \frac{1}{r} \frac{\partial \langle v_r \rangle^{(0)}}{\partial \theta} + r \frac{\partial}{\partial r} \left( \frac{\langle v_\theta \rangle^{(0)}}{r} \right) \right). \end{aligned} \quad (\text{A66})$$

Combining the above equations we obtain

$$\begin{aligned} \frac{\partial P^{(1)}}{\partial r} &= 2 \frac{\partial}{\partial r} \left( \frac{1}{r} \frac{\partial}{\partial r} \left( r \langle v_r \rangle^{(0)} \right) \right) + \frac{\partial}{\partial r} \left( \frac{1}{r} \frac{\partial \langle v_\theta \rangle^{(0)}}{\partial \theta} \right) + \frac{1}{r^2} \frac{\partial^2 \langle v_r \rangle^{(0)}}{\partial \theta^2} - \frac{2}{r^2} \frac{\partial \langle v_\theta \rangle^{(0)}}{\partial \theta} \\ &+ \frac{2}{h^{(0)}} \frac{\partial h^{(0)}}{\partial r} \left( \frac{1}{r} \frac{\partial}{\partial r} \left( r \langle v_r \rangle^{(0)} \right) + \frac{\partial \langle v_r \rangle^{(0)}}{\partial r} + \frac{1}{r} \frac{\partial \langle v_\theta \rangle^{(0)}}{\partial \theta} \right) \\ &+ \frac{1}{h^{(0)}} \frac{1}{r} \frac{\partial h^{(0)}}{\partial \theta} \left( \frac{1}{r} \frac{\partial \langle v_r \rangle^{(0)}}{\partial \theta} + r \frac{\partial}{\partial r} \left( \frac{\langle v_\theta \rangle^{(0)}}{r} \right) \right), \end{aligned} \quad (\text{A67})$$

$$\begin{aligned} \frac{1}{r} \frac{\partial P^{(1)}}{\partial \theta} &= \frac{2}{r^2} \frac{\partial^2 \langle v_\theta \rangle^{(0)}}{\partial \theta^2} + \frac{\partial}{\partial r} \left( \frac{1}{r} \frac{\partial}{\partial r} (r \langle v_\theta \rangle^{(0)}) \right) + \frac{1}{r} \frac{\partial}{\partial \theta} \left( \frac{1}{r} \frac{\partial}{\partial r} (r \langle v_r \rangle^{(0)}) \right) \\ &+ \frac{2}{r^2} \frac{\partial \langle v_r \rangle^{(0)}}{\partial \theta} + \frac{2}{h^{(0)}} \frac{1}{r} \frac{\partial h^{(0)}}{\partial \theta} \left( \frac{1}{r} \frac{\partial}{\partial r} (r \langle v_r \rangle^{(0)}) + \frac{\langle v_r \rangle^{(0)}}{r} + \frac{2}{r} \frac{\partial \langle v_\theta \rangle^{(0)}}{\partial \theta} \right) \\ &+ \frac{1}{h^{(0)}} \frac{\partial h^{(0)}}{\partial r} \left( \frac{1}{r} \frac{\partial \langle v_r \rangle^{(0)}}{\partial \theta} + r \frac{\partial}{\partial r} \left( \frac{\langle v_\theta \rangle^{(0)}}{r} \right) \right). \end{aligned} \tag{A68}$$

A.1.7. Combine  $O(1)$  and  $O(\epsilon)$  equations

To regularize the  $O(1)$  equations, we introduce the following set of combined variables:  $\hat{h} = h^{(0)} + \epsilon h^{(1)}$ ,  $\hat{h}_1 = h_1^{(0)} + \epsilon h_1^{(1)}$ ,  $\widehat{v_r} = \langle v_r \rangle^{(0)} + \epsilon \langle v_r \rangle^{(1)}$ ,  $\widehat{v_\theta} = \langle v_\theta \rangle^{(0)} + \epsilon \langle v_\theta \rangle^{(1)}$  and  $\hat{P} = \mathcal{P}^{(0)} + \epsilon P^{(1)}$ . The governing equations are as follows:

$$\frac{\partial \hat{h}}{\partial t} + \frac{1}{r} \frac{\partial}{\partial r} (r \hat{h} \widehat{v_r}) + \frac{1}{r} \frac{\partial \hat{h} \widehat{v_\theta}}{\partial \theta} = 0, \tag{A69}$$

$$\begin{aligned} \frac{\partial c^{(0)}}{\partial t} + \langle v_r \rangle^{(0)} \frac{\partial c^{(0)}}{\partial r} + \langle v_\theta \rangle^{(0)} \frac{1}{r} \frac{\partial c^{(0)}}{\partial \theta} - \frac{1}{Pe} \left( \frac{1}{r} \frac{\partial}{\partial r} \left( r \frac{\partial c^{(0)}}{\partial r} \right) + \frac{1}{r^2} \frac{\partial^2 c^{(0)}}{\partial \theta^2} \right) \\ - \frac{1}{Pe} \frac{1}{\hat{h}} \left( \frac{\partial \hat{h}}{\partial r} \frac{\partial c^{(0)}}{\partial r} + \frac{1}{r} \frac{\partial \hat{h}}{\partial \theta} \frac{1}{r} \frac{\partial c^{(0)}}{\partial \theta} \right) = -\frac{2\beta}{\hat{h}} j_n, \end{aligned} \tag{A70}$$

$$\frac{\partial \Gamma^{(0)}}{\partial t} + \frac{1}{r} \frac{\partial}{\partial r} (r \Gamma^{(0)} v_{r,s}) + \frac{1}{r} \frac{\partial}{\partial \theta} (\Gamma^{(0)} v_{\theta,s}) - \frac{1}{Pe_S} \left( \frac{1}{r} \frac{\partial}{\partial r} \left( r \frac{\partial \Gamma^{(0)}}{\partial r} \right) + \frac{1}{r^2} \frac{\partial^2 \Gamma^{(0)}}{\partial \theta^2} \right) = j_n, \tag{A71}$$

$$\frac{1}{r} \frac{\partial}{\partial r} \left( r \frac{\partial \hat{h}_1}{\partial r} \right) + \frac{1}{r^2} \frac{\partial^2 \hat{h}_1}{\partial \theta^2} - Bo \hat{h}_1 = -Ca \hat{P} - 2\epsilon Ca \left( \frac{1}{r} \frac{\partial}{\partial r} (r \widehat{v_r}) + \frac{1}{r} \frac{\partial \widehat{v_\theta}}{\partial \theta} \right), \tag{A72}$$

$$\begin{aligned} \frac{\partial \hat{P}}{\partial r} &= \frac{1}{\hat{h}} \frac{2}{\epsilon Ca} \frac{\partial - \Pi^{(0)}}{\partial r} \\ &+ \epsilon \left[ 2 \frac{\partial}{\partial r} \left( \frac{1}{r} \frac{\partial}{\partial r} (r \widehat{v_r}) \right) + \frac{\partial}{\partial r} \left( \frac{1}{r} \frac{\partial \widehat{v_\theta}}{\partial \theta} \right) + \frac{1}{r^2} \frac{\partial^2 \widehat{v_r}}{\partial \theta^2} - \frac{2}{r^2} \frac{\partial \widehat{v_\theta}}{\partial \theta} \right. \\ &+ \frac{2}{\hat{h}} \frac{\partial \hat{h}}{\partial r} \left( \frac{1}{r} \frac{\partial}{\partial r} (r \widehat{v_r}) + \frac{\partial \widehat{v_r}}{\partial r} + \frac{1}{r} \frac{\partial \widehat{v_\theta}}{\partial \theta} \right) \\ &\left. + \frac{1}{\hat{h}} \frac{1}{r} \frac{\partial \hat{h}}{\partial \theta} \left( \frac{1}{r} \frac{\partial \widehat{v_r}}{\partial \theta} + r \frac{\partial}{\partial r} \left( \frac{\widehat{v_\theta}}{r} \right) \right) \right], \end{aligned} \tag{A73}$$

## Instability of surfactant films

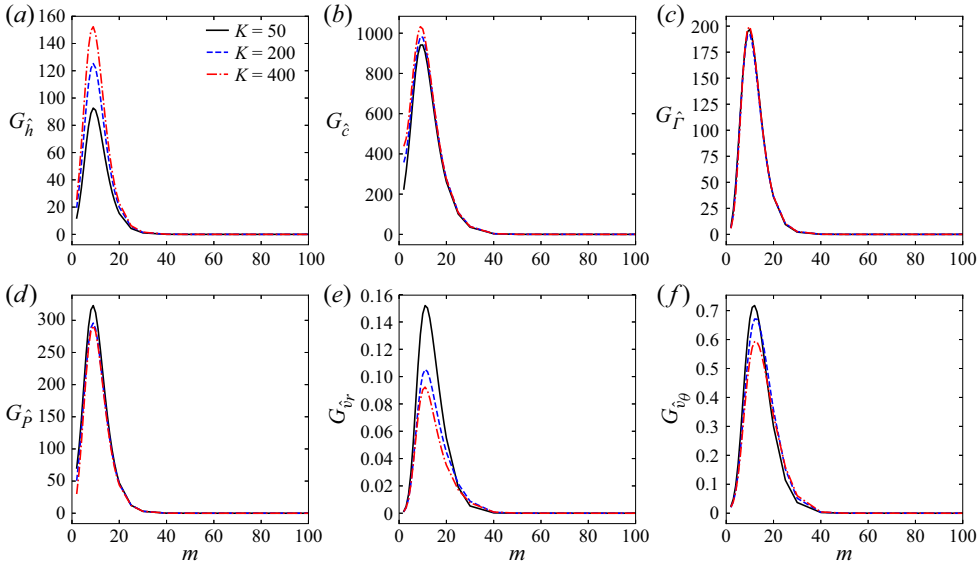


Figure 14. Effects of varying the exponential factor,  $K$ , on linearized disturbance quantities at  $t = 4.05$ . For this set of simulations,  $t_{stop} = 3.11$  and  $t_{ini} = 4$ . All other parameters used in the linear stability analysis are the same as those in figure 8.

$$\begin{aligned}
 \frac{1}{r} \frac{\partial \hat{P}}{\partial \theta} &= \frac{1}{\hat{h}} \frac{2}{\epsilon Ca r} \frac{\partial - \Pi^{(0)}}{\partial \theta} \\
 &+ \epsilon \left[ \frac{2}{r^2} \frac{\partial^2 \langle \widehat{v}_\theta \rangle}{\partial \theta^2} + \frac{\partial}{\partial r} \left( \frac{1}{r} \frac{\partial}{\partial r} (r \langle \widehat{v}_\theta \rangle) \right) + \frac{1}{r} \frac{\partial}{\partial \theta} \left( \frac{1}{r} \frac{\partial}{\partial r} (r \langle \widehat{v}_r \rangle) \right) + \frac{2}{r^2} \frac{\partial \langle \widehat{v}_r \rangle}{\partial \theta} \right. \\
 &+ \frac{2}{\hat{h}} \frac{1}{r} \frac{\partial \hat{h}}{\partial \theta} \left( \frac{1}{r} \frac{\partial}{\partial r} (r \langle \widehat{v}_r \rangle) + \frac{\langle \widehat{v}_r \rangle}{r} + \frac{2}{r} \frac{\partial \langle \widehat{v}_\theta \rangle}{\partial \theta} \right) \\
 &\left. + \frac{1}{\hat{h}} \frac{\partial \hat{h}}{\partial r} \left( \frac{1}{r} \frac{\partial \langle \widehat{v}_r \rangle}{\partial \theta} + r \frac{\partial}{\partial r} \left( \frac{\langle \widehat{v}_\theta \rangle}{r} \right) \right) \right]. \tag{A74}
 \end{aligned}$$

### A.2. Variations of the initial disturbance

The exponential factor  $K$  in (4.10) and (4.11) are varied for the case studied in figure 8. For  $K = 50$ ,  $K = 200$  and  $K = 400$ , the gain for the six linearized disturbance quantities are plotted over a range of wavenumbers (figure 14). For the three values of  $K$  examined, there is no significant change in the most dangerous wavenumber that grows the fastest.

### A.3. Fourier transform of experimental rim locations

Figures 15(a) and 15(c) show the Fourier transform of the rim location for two experiments conducted at different  $t_{stop}$  values. The time rate of change in the prominent Fourier signals are displayed in figures 15(b) and 15(d). The two fastest growing wavenumbers for each experiment are used as validation data in figure 13.

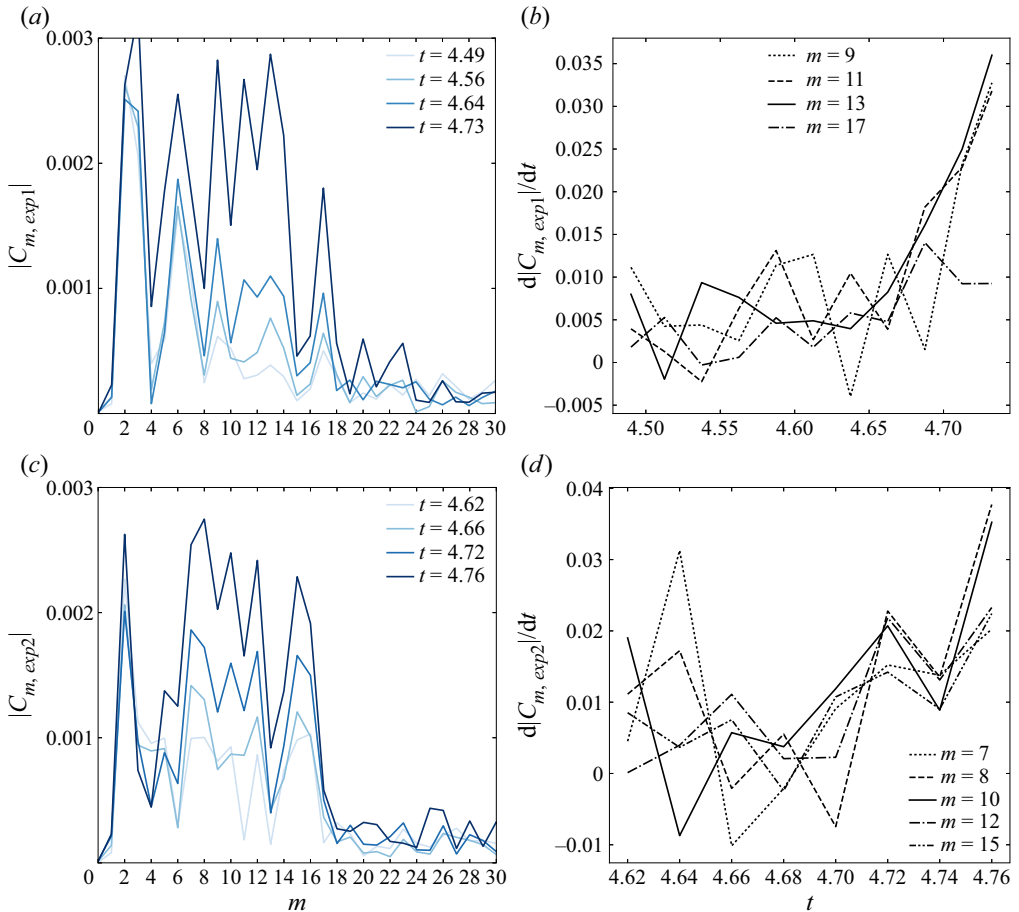


Figure 15. (a,c) Fourier transform of the rim location during symmetry breaking for experiment 1 (a) and experiment 2 (c). (b,d) Time rate of change in the amplitude of the Fourier signals for selected wavenumbers for experiment 1 (b) and experiment 2 (d). The experimental conditions are described in figure 13.

In figures 15(a) and 15(c) the last time step plotted corresponds to the time at which the location of the rim stays within the field of view of the top camera. Beyond that time, the location of the rim evolves beyond the field of view and  $R(\theta)$  is not defined for  $\theta \in [0, 2\pi)$ , which is required for the Fourier analysis used in this study.

#### REFERENCES

- ATASI, O., LEGENDRE, D., HAUT, B., ZENIT, R. & SCHEID, B. 2020 Lifetime of surface bubbles in surfactant solutions. *Langmuir* **36** (27), 7749–7764.
- BALAY, S., *et al.* 2019 PETSc users manual. <http://www.mcs.anl.gov/petsc/petsc-current/docs/manual.pdf>
- BARAKAT, J.M. 2018 Microhydrodynamics of vesicles in channel flow. PhD thesis. Stanford University.
- BHAMLA, M.S., CHAI, C., ALVAREZ-VALENZUELA, M., TAJUELO, J. & FULLER, G.G. 2017 Interfacial mechanisms for stability of surfactant-laden films. *PLoS One* **12** (5), e0175753.
- BORKOWSKI, M., KOSIOR, D. & ZAWALA, J. 2020 Effect of initial adsorption coverage and dynamic adsorption layer formation at bubble surface in stability of single foam films. *Colloids Surf. (A)* **589**, 124446.
- CHAMPOUGNY, L., ROCHÉ, M., DRENCKHAN, W. & RIO, E. 2016 Life and death of not so “bare” bubbles. *Soft Matt.* **12** (24), 5276–5284.

- CHANG, C. & FRANSES, E.I. 1995 Adsorption dynamics of surfactants at the air/water interface: a critical review of mathematical models, data, and mechanisms. *Colloids Surf. (A)* **100**, 1–45.
- CHATZIGIANNAKIS, E., JAENSSON, N. & VERMANT, J. 2021 Thin liquid films: where hydrodynamics, capillarity, surface stresses, and intermolecular forces meet. *Curr. Opin. Colloid Interface Sci.* **53**, 101441.
- CUNLIFFE, M., ENGEL, A., FRKA, S., GAŠPAROVIĆ, B., GUITART, C., MURRELL, J.C., SALTER, M., STOLLE, C., UPSTILL-GODDARD, R. & WURL, O. 2013 Sea surface microlayers: a unified physicochemical and biological perspective of the air–ocean interface. *Prog. Oceanogr.* **109**, 104–116.
- DAVE, D. & GHALY, A.E. 2011 Remediation technologies for marine oil spills: a critical review and comparative analysis. *Am. J. Environ. Sci.* **7** (5), 423–440.
- FROSTAD, J.M., TAMMARO, D., SANTOLLANI, L., DE ARAUJO, S.B. & FULLER, G.G. 2016 Dynamic fluid–film interferometry as a predictor of bulk foam properties. *Soft Matt.* **12** (46), 9266–9279.
- GROS, A., BUSSONNIÈRE, A., NATH, S. & CANTAT, I. 2021 Marginal regeneration in a horizontal film: instability growth law in the nonlinear regime. *Phys. Rev. Fluids* **6** (2), 024004.
- HELLGREN, A., WEISSENBORN, P. & HOLMBERG, K. 1999 Surfactants in water-borne paints. *Prog. Org. Coat.* **35** (1–4), 79–87.
- HERMANS, E., BHAMLA, M.S., KAO, P., FULLER, G.G. & VERMANT, J. 2015 Lung surfactants and different contributions to thin film stability. *Soft Matt.* **11** (41), 8048–8057.
- JENSEN, O.E. & NAIRE, S. 2006 The spreading and stability of a surfactant-laden drop on a prewetted substrate. *J. Fluid Mech.* **554**, 5–24.
- JOYE, J. 1994 Mechanisms of symmetric and asymmetric drainage of foam films. PhD thesis, Rice University.
- LHUISSIER, H. & VILLERMAUX, E. 2012 Bursting bubble aerosols. *J. Fluid Mech.* **696**, 5–44.
- LIN, S., MCKEIGUE, K. & MALDARELLI, C. 1990 Diffusion-controlled surfactant adsorption studied by pendant drop digitization. *AIChE J.* **36** (12), 1785–1795.
- MIGUET, J., PASQUET, M., ROUYER, F., FANG, Y. & RIO, E. 2021 Marginal regeneration-induced drainage of surface bubbles. *Phys. Rev. Fluids* **6** (10), L101601.
- OCHOA, C., GAO, S., SRIVASTAVA, S. & SHARMA, V. 2021 Foam film stratification studies probe intermicellar interactions. *Proc. Natl Acad. Sci. USA* **118** (25), e2024805118.
- PIGEONNEAU, F. & SELLIER, A. 2011 Low-Reynolds-number gravity-driven migration and deformation of bubbles near a free surface. *Phys. Fluids* **23** (9), 092102.
- POULAIN, S., VILLERMAUX, E. & BOUROUIBA, L. 2018 Ageing and burst of surface bubbles. *J. Fluid Mech.* **851**, 636–671.
- SHEN, A.Q., GLEASON, B., MCKINLEY, G.H. & STONE, H.A. 2002 Fiber coating with surfactant solutions. *Phys. Fluids* **14** (11), 4055–4068.
- SHI, X., FULLER, G.G. & SHAQFEH, E.S.G. 2020 Oscillatory spontaneous dimpling in evaporating curved thin films. *J. Fluid Mech.* **889**, A25.
- SHI, X., RODRÍGUEZ-HAKIM, M., SHAQFEH, E.S.G. & FULLER, G.G. 2021 Instability and symmetry breaking in binary evaporating thin films over a solid spherical dome. *J. Fluid Mech.* **915**, A45.
- STUBENRAUCH, C. & VON KLITZING, R. 2003 Disjoining pressure in thin liquid foam and emulsion films—new concepts and perspectives. *J. Phys.: Condens. Matter* **15** (27), R1197.
- TAGAWA, Y., TAKAGI, S. & MATSUMOTO, Y. 2014 Surfactant effect on path instability of a rising bubble. *J. Fluid Mech.* **738**, 124–142.
- WARNER, M.R.E., CRASTER, R.V. & MATAR, O.K. 2004 Fingering phenomena created by a soluble surfactant deposition on a thin liquid film. *Phys. Fluids* **16** (8), 2933–2951.
- ZASADZINSKI, J.A., DING, J., WARRINER, H.E., BRINGEZU, F. & WARING, A.J. 2001 The physics and physiology of lung surfactants. *Curr. Opin. Colloid Interface Sci.* **6** (5–6), 506–513.